TZIMI NIKI

NATIONAL TECHNICAL UNIVERSITY OF ATHENS

Engineering models for the analysis of Vortex – Induced Vibrations

Department: Fluid Dynamics

Supervisor: Vasileios Riziotis

Athens 2024

Acknowledgments

First of all, I would like to sincerely thank my professor Vasileios Riziotis for his continuous advice and support throughout this thesis. His patience, time management skills, and understanding of the project's needs were truly inspiring and served as a constant source of motivation.

I am also grateful to Dimitris Vlastos, a Ph.D. candidate under the guidance of professor Vasileios Riziotis. His guidance and assistance were crucial in overcoming obstacles encountered during my thesis.

Finally, a big thank you to my parents, my sister, my friends, and Vasilis for their unwavering support and encouragement.

Abstract

The thesis presents a comprehensive investigation of the vortex-induced vibration (VIV) phenomenon in circular cross-section structures, employing both single-single-degree-of-freedom (1DOF) and two-degree-of-freedom (2DOF) engineering models. The primary objectives revolve around understanding, analyzing, and predicting VIV behavior across a range of flow velocities.

To achieve this goal, the study evaluates both single-degree-of-freedom (1DOF) and two-degree-of-freedom (2DOF) engineering models, assessing their efficacy in predicting VIV behavior. Through meticulous evaluation against theoretical predictions and experimental data, a newly proposed 1DOF model from existing literature aligns well with the theoretical predictions, indicating its accuracy.

Furthermore, the thesis explores optimization techniques for fine-tuning the parameters of the 2DOF models, with the COBYLA method demonstrating superior accuracy over the Newton method. The model's results were tested across different frequency ratio cases, revealing a subtle leftward shift in maximum amplitude values. Additionally, an automated method was examined, defining the parameters' optimal values and applying linear interpolation for predictions in the lock-in region.

The findings emphasize the importance of accurate prediction methodologies for VIV phenomena and highlight future research, such as exploring additional optimization methods and engineering models. Moreover, the integration of these results into computational tools, such as the hGAST tool for offshore wind turbine analysis, offers practical applications for large-scale engineering structures with complex dynamics.

In summary, this thesis contributes to enhancing the understanding and prediction capabilities of VIV phenomena, offering valuable insights for structural analysis in various fields, including offshore structures, wind turbines, and marine engineering.

Abstract (in Greek)

Η διπλωματική εργασία παρουσιάζει μια ολοκληρωμένη διερεύνηση του φαινομένου των ταλαντώσεων που προκαλούνται από δίνες (VIV) σε κατασκευές κυκλικής διατομής, χρησιμοποιώντας τόσο μηχανικά μοντέλα ενός βαθμού ελευθερίας (1DOF) όσο και δύο βαθμών ελευθερίας (2DOF). Οι πρωταρχικοί στόχοι περιστρέφονται γύρω από την κατανόηση, την ανάλυση και την πρόβλεψη της συμπεριφοράς του φαινομένου σε ένα εύρος ταχυτήτων ροής.

Για την επίτευξη αυτού του στόχου, η μελέτη αξιολογεί τόσο τα μοντέλα ενός βαθμού ελευθερίας (1DOF) όσο και τα μοντέλα δύο βαθμών ελευθερίας (2DOF), αξιολογώντας την αποτελεσματικότητά τους στην πρόβλεψη της συμπεριφοράς του φαινομένου. Μέσω σύγκρισης έναντι θεωρητικών προβλέψεων και πειραματικών δεδομένων, ένα προτεινόμενο μοντέλο 1DOF από την υπάρχουσα βιβλιογραφία ευθυγραμμίζεται καλά με τις θεωρητικές προβλέψεις, υποδεικνύοντας την ακρίβειά του.

Επιπλέον, η διπλωματική εργασία διερευνά τεχνικές βελτιστοποίησης για τη λεπτομερή ρύθμιση των παραμέτρων του μοντέλου 2DOF, με τη μέθοδο COBYLA να επιδεικνύει ανώτερη ακρίβεια σε σχέση με τη μέθοδο Newton. Τα αποτελέσματα του μοντέλου δοκιμάστηκαν σε διαφορετικές περιπτώσεις αναλογίας συχνοτήτων, αποκαλύπτοντας μια ελαφρά μετατόπιση προς τα αριστερά στην τιμή του μέγιστου πλάτους. Επιπλέον, εξετάστηκε μια αυτοματοποιημένη μέθοδος, η οποία καθόριζε τις βέλτιστες τιμές των παραμέτρων και εφάρμοζε γραμμική παρεμβολή για προβλέψεις στην περιοχή lock-in.

Τα ευρήματα υπογραμμίζουν τη σημασία των μεθοδολογιών πρόβλεψης με ακρίβεια για τα φαινόμενα VIV και ενθαρρύνουν μελλοντική έρευνα ως προς τη διερεύνηση πρόσθετων μεθόδων βελτιστοποίησης και τεχνικών μοντέλων. Επιπλέον, η ενσωμάτωση αυτών των αποτελεσμάτων σε υπολογιστικά εργαλεία, όπως το εργαλείο hGAST για την ανάλυση υπεράκτιων ανεμογεννητριών, προσφέρει πρακτικές εφαρμογές για μηχανικές κατασκευές μεγάλης κλίμακας.

Συνοπτικά, η παρούσα εργασία συμβάλλει στην ενίσχυση της κατανόησης και της δυνατότητας πρόβλεψης των φαινομένων VIV, προσφέροντας πολύτιμες γνώσεις για τη δομική ανάλυση σε διάφορους τομείς, συμπεριλαμβανομένων των υπεράκτιων κατασκευών, των ανεμογεννητριών και της θαλάσσιας μηχανικής.

Table of Contents

1. Introduction

1.1 Objectives

The primary objectives of this thesis work revolve around a comprehensive study, analysis, and understanding of the vortex-induced vibration (VIV) phenomenon. Recognizing its complex nature, the aim is to approach this phenomenon with a quick and accurate method.

While computational fluid dynamics (CFD) presents a way for precise investigation of VIVs, its excessive computational cost in terms of both time and resources poses significant constraints. Therefore, a pivotal objective of this study is to explore alternative methods, particularly the application of engineering models, including both single-degree-of-freedom (1DOF) and two-degree-of-freedom (2DOF) models, that offer a balance between computational efficiency and analytical accuracy.

The 1DOF models, consisting of three distinct variations sourced from existing literature, will undergo a meticulous evaluation to ensure their efficacy in predicting VIVs by comparing their results with experimental data. The 2DOF model, on the other hand, will also be subjected to calibration through the process of adjusting and fine-tuning the model parameters to enhance their accuracy and reliability in predicting the phenomenon.

Furthermore, given the widespread occurrence of VIVs across various engineering applications, the thesis will focus specifically on cylindrical cross-sections, representing structures such as wind turbine towers, chimneys, cylindrical towers, and marine structures. Ultimately, the utilization of these models is anticipated to significantly reduce the computational cost of subsequent aeroelastic analysis while they are expected to facilitate a thorough understanding of the VIV phenomenon.

1.2 Understanding Vortex-Induced Vibrations Phenomenon

Vortex-induced vibrations (VIVs) represent a complex phenomenon that intersects various disciplines, including fluid mechanics, structural mechanics, vibrations, computational fluid dynamics (CFD), and acoustics. This intricate interaction occurs in numerous engineering applications, from bridges and offshore structures to marine cables and industrial chimneys. As technological advancements and material science have evolved, there has been a notable increase in the height and slenderness of structures. Consequently, these modern structures are more susceptible to VIV phenomena. Understanding and predicting VIV is crucial, aiming

to mitigate potential structure fatigue and failure. [1] It is more advantageous to predict and consequently avoid the VIVs than to attempt to eliminate them. [2]

Wind action plays a significant role in structural dynamics and it can be divided into two groups: aerodynamic and aeroelastic. While aerodynamic effects on structures are independent of their movement, aeroelastic effects are affected by structural vibration. Flutter, galloping and vortex shedding are examples of aeroelastic actions. [3] Vortex-induced vibrations (VIVs) are structural vibrations that can occur due to the shedding of flow vortices when a fluid flow passes around a structure. Due to this fluid-structure interaction (FSI) phenomenon, a synchronization (also called lock-in) of the vortex shedding and the structural motion can occur for certain flow conditions and structural properties. [4]

Synchronization, also known as lock-in, (or lock-on, vortex capture, or frequency capture), is observed not only in the vicinity of the natural frequency of the structure but also across a broad spectrum of flow velocities. Beyond the synchronization region, the body will encounter forces characterized by both the Strouhal frequency and the frequency of body oscillations. [2] The study of VIVs is about bluff bodies, typically circular cylinders. [5]

Analyzing the behavior of an elastically mounted cylinder constrained to move perpendicular to the flow and reach the lock-in region, distinct wake patterns can be initiated by the motion of the body. [6] Various vortex wake patterns are identified and introduced, across a wide range of amplitudes and wavelengths. These periodic wake patterns consist of single vortices (S) and vortex pairs (P), resulting in modes such as $2S$, $2P$, and $P + S$, which are the predominant modes near the lock-in region. [7]
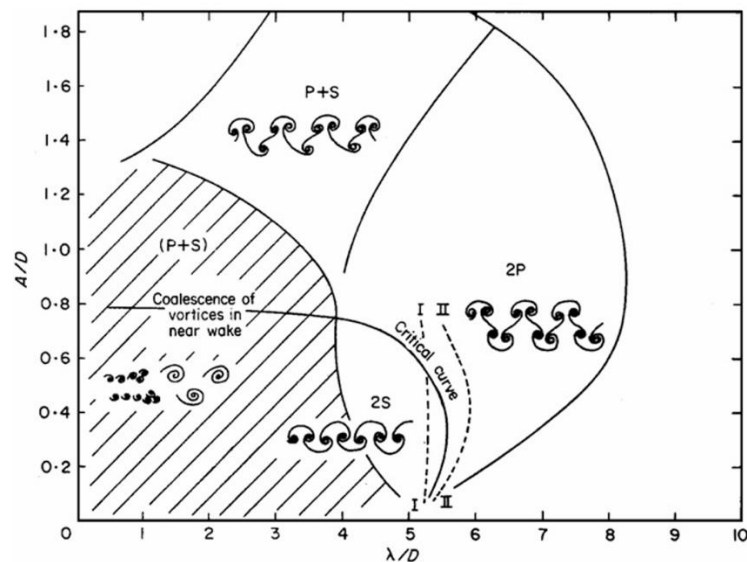

Image 1: Visualization of vortex wake modes

Studies using flow visualization techniques [8] [9] have revealed that initially, vortices form on one side of the cylinder and are shed when the cylinder is near maximum displacement on the opposite side. Towards the end of the lock-in range, however, vortices are shed when the cylinder is near maximum displacement on the same side. These observations underscore the complex dynamics in the VIV phenomenon, where subtle variations in flow conditions and cylinder motion lead to distinct modes of vortex shedding.
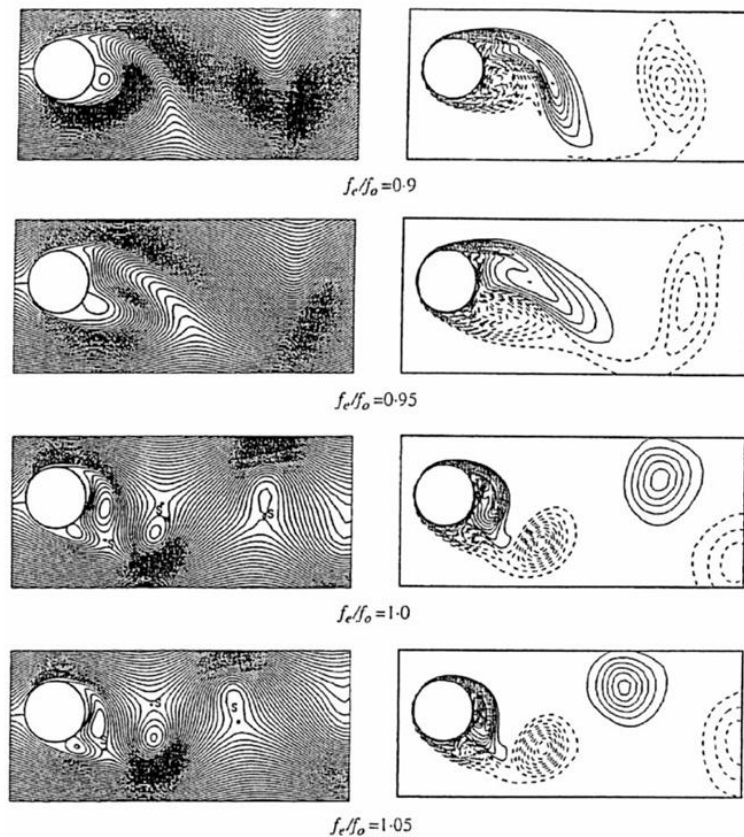
Image 2: Evolution of vortex shedding patterns at varying lock-in ratios. At ratio 0.95, a new vortex emerges from the upper surface of the cylinder, while at ratio 1.0 the shedding transitions to the lower surface.

Significant progress has been achieved in elucidating the kinematics of VIVs, particularly in the low-Reynolds number regime. [10] [11] However, challenges persist due to many factors influencing the phenomenon, including lift coefficient, correlation length, the vortex-shedding frequency, Reynolds number, and the vortex-shedding frequency bandwidth. [12] Nonetheless, the Strouhal number emerges as a robust parameter despite these complexities. [2] The Strouhal number is influenced by factors such as the structure's geometry, Reynolds number, and air turbulence levels and it measures the geometry of the vortex wake as illustrated in Image 3. [13]

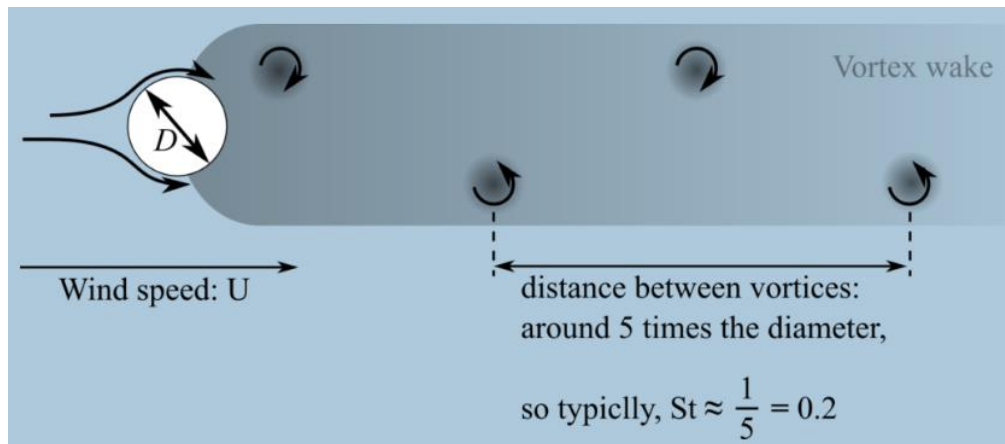**Image 3: Typical value of Strouhal number for circular cylinders**

Furthermore, the correlation between the Strouhal and Reynolds numbers, as depicted in Image 4, offers valuable insights into the behavior of the Strouhal number for circular cylinders across different flow regimes, from subcritical to supercritical. [14]
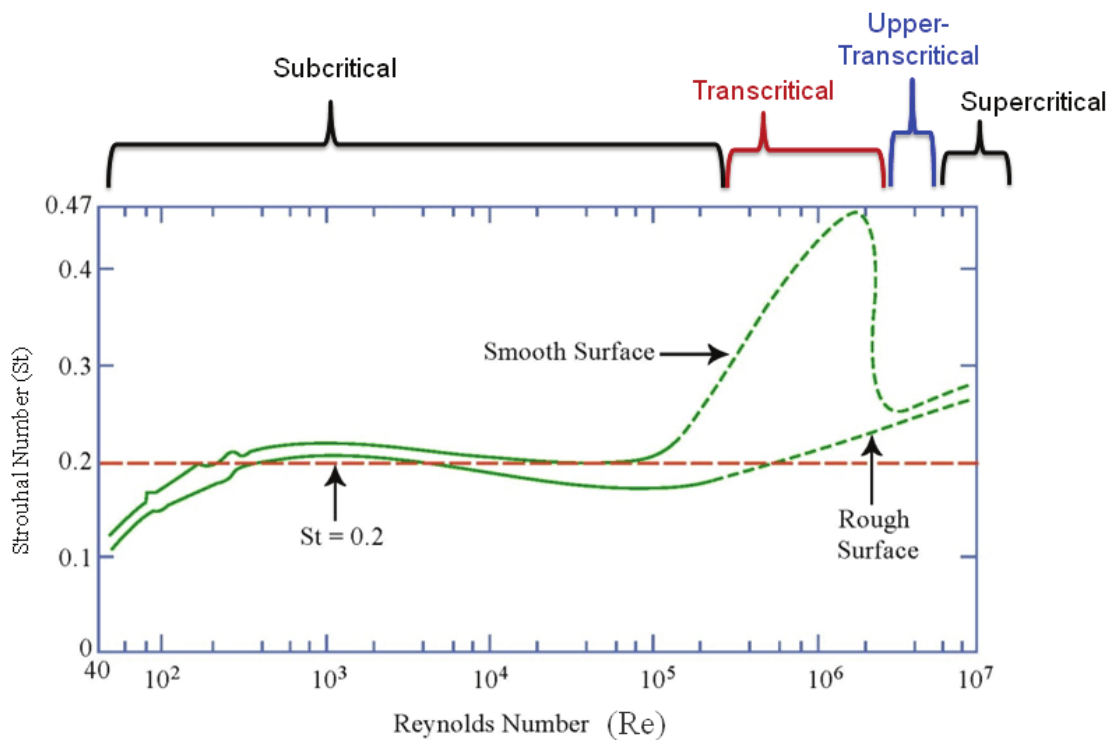
Image 4: Correlation between Strouhal and Reynolds numbers for circular cylinders

Another parameter that provides valuable insights into the phenomenon of vortex-induced vibrations, is the mass-damping parameter, also known as the Scruton number.

$$Sc = \frac{\zeta m}{\rho D^2}$$

$$(1.1)$$

This parameter hinges on two critical properties: the damping of the structure, ζ and its relative mass, m, compared to the surrounding air. [13] Structures with higher structural damping exhibit reduced vibrations compared to those with lower. Similarly, heavier structures experience less severe vibrations than lighter structures. However, these vibrations tend to exhibit irregular patterns, with occasional bursts of slightly larger oscillations. The relationship between the Scruton number and vibration amplitude is depicted in Image 5.

Image 5: Scruton curve, also known as Griffin plot

2. Theoretical Presentation of Basic Engineering Models

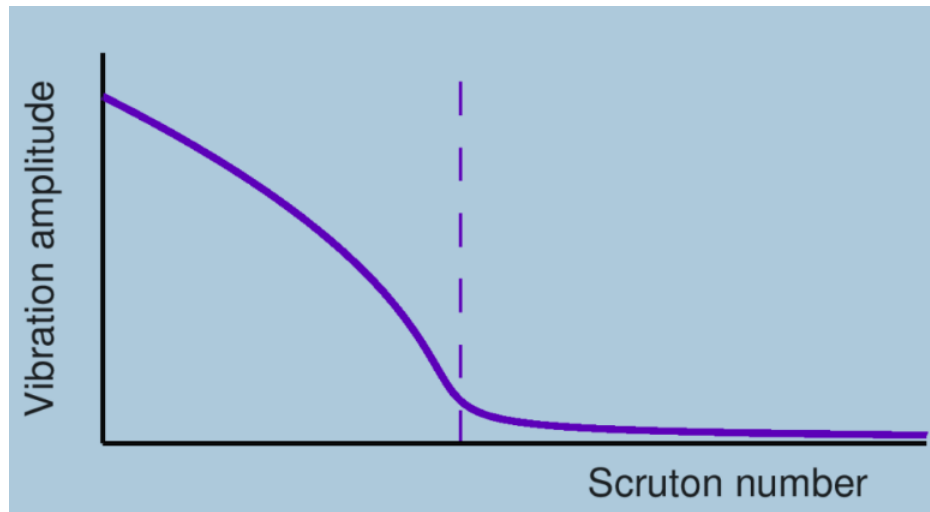VIV poses significant challenges across a spectrum of engineering domains, including aerospace, civil, wind, and industrial engineering applications. [15] Understanding and predicting these vibrations is crucial for ensuring the structural integrity and operational efficiency of such systems. Over the years, various engineering mathematical models have been developed to analyze and quantify VIV phenomena. In the following chapter, several engineering models will be explored to present their theoretical foundations and mathematical formulations.

Two classes of VIV models exist the 1-degree-of-freedom models and the coupled wake oscillator models, each offering distinct approaches to modeling VIV phenomena. [16] There are various proposals from different authors to model the phenomenon of vortex shedding, all originating from the simple case of two-dimensional flow. Analytical, empirical, and semi-empirical models are among the methods applied. The commonly adopted approach involves constructing empirical models and subsequently refining their results to align with real-world observations through a selection of parameters. [3]

2.1 Iwan-Blevins Model

The Iwan–Blevins model, proposed by Iwan and Blevins in 1974, offers a mathematical framework for understanding vortex-induced vibrations (VIV) in structures. [17] At its core, the model introduces a "hidden" fluid variable represented by z, where the time derivative $\dot{z}$ describes how the sideways or lateral motion of fluid changes over time within a specified area. This variable is directly proportional to the momentum within the control volume, as illustrated in Image 6.
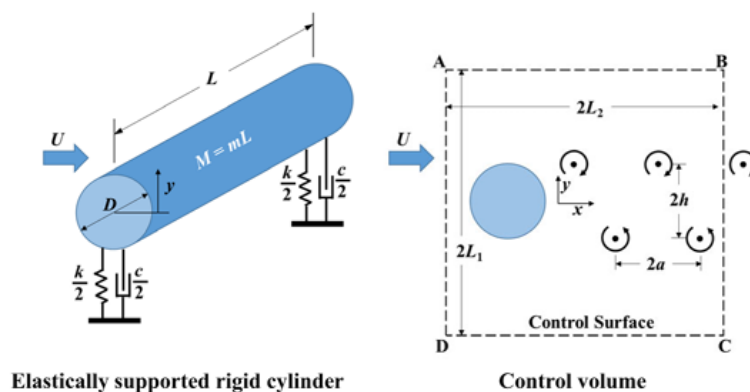

Elastically supported rigid cylinder   Control volume

Image 6: Illustration of the fluid variable z and its role in capturing fluid motion within a defined control volume

By deriving a fluid oscillator from the momentum equation in the transverse direction, the model incorporates a $\dot{z}^3$ term to capture non-linear features inherent in VIV phenomena. This non-linearity enables the model to effectively replicate the intricate dynamics of vortex-induced vibrations. The self-excited fluid oscillator is expressed by the following equation:

$$\ddot{z} + K'\frac{u_t}{D}\omega_v z = (a_1' - a_4')\frac{U}{D}\dot{z} - a_2'\frac{\dot{z}^3}{UD} + a_3'\ddot{y} + a_4'\frac{U}{D}\dot{y} \tag{2.1}$$

Where

$$K' = \frac{K}{a_0 + a_3} \quad and \quad a_i' = \frac{a_i}{a_0 + a_3} \quad (i = 3; 4)$$

The cylinder movement equation is given by:

$$\ddot{y} + 2\xi_T\omega_y\dot{y} + \omega_y^2 y = a_3''\ddot{z} + a_4''\dot{z}\frac{U}{D} \tag{2.2}$$

Where

$$\omega_y = \frac{\sqrt{\frac{k}{m}}}{1 + \frac{a_3\rho D^2}{m}}, \qquad \xi_T = \frac{\xi\frac{\sqrt{\frac{k}{m}}}{\omega_y} + \frac{a_4\rho DU}{2m\omega_y}}{1 + \frac{a_3\rho D^2}{m}}, \qquad a_i'' = \frac{\rho D^2 a_i}{m + a_3\rho D^2} \quad (i = 3; 4)$$

Experimental validation of the Iwan–Blevins model against circular cylinder responses, highlights its ability to accurately predict maximum response amplitudes as shown in Image 7. However, a notable discrepancy arises in the timing of peak responses between the model predictions and experimental observations. While the model accurately predicts maximum response amplitudes at the resonant flow velocity U_R, experimental data exhibit a delay, reaching maximum amplitude at around $1.15U_R$. This discrepancy, particularly pronounced in light-weight and low-damping cylinder cases, constitutes a limitation of the model in capturing certain details of VIV behavior.

Despite this limitation, the Iwan–Blevins model successfully reproduces the frequency lock-in phenomenon observed in VIV. Image 7 illustrates the model's ability to capture this characteristic feature, albeit with a narrower lock-in region compared to experimental results. Additionally, experimental observations reveal that when the structural damping factor ζ_s surpasses the fluid damping factor ζ_f, a common situation in practical applications, the model anticipates a widening of the entrainment band. This widening effect is directly proportional to the ratio of the displaced fluid mass to the cylinder mass. Notably, when this ratio increases, structures oscillating in denser fluids, such as water, would exhibit a broader entrainment band compared to those oscillating in less dense fluids, like air. [18]
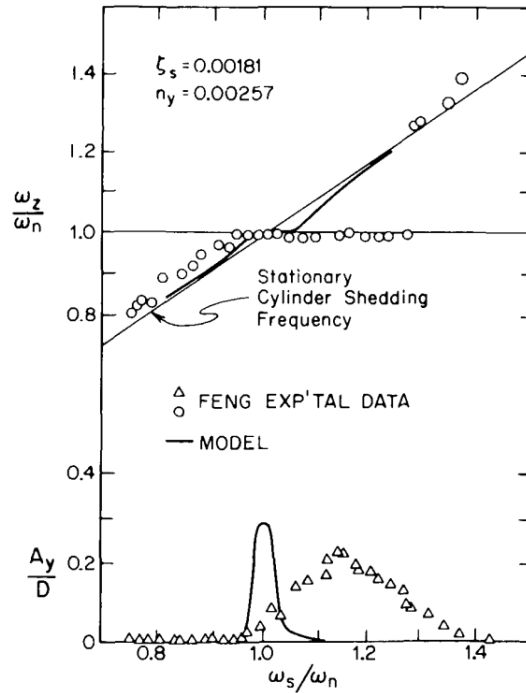
Image 7: Comparison between experimental and model-predicted responses of a circular cylinder
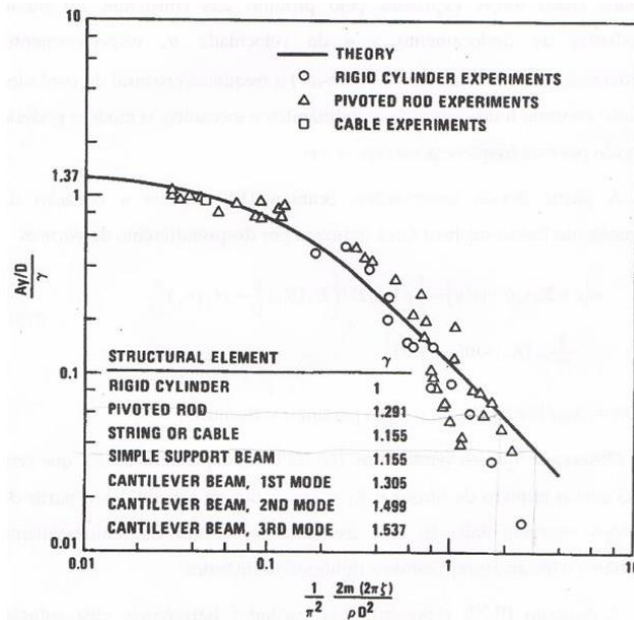

Image 8: Amplitude variations for rigid and structurally elastic cylinders according to the damping parameter

Additionally, Image 8 presents a comparison between theoretical predictions and experimental results, specifically focusing on the amplitude variations for different cylinder types as influenced by the damping parameter. [19]

2.2 Modified coupled van der Pol Model

The modified coupled van der Pol (VDP) wake oscillator model provides an innovative approach that combines elements of the van der Pol oscillator with a spring-mass-damper system and applies to two-dimensional scenarios, with a particular emphasis on circular cylinders constrained to transverse motion. [20] Represented as a single-degree-of-freedom model, its graphical depiction is illustrated in Image 9.

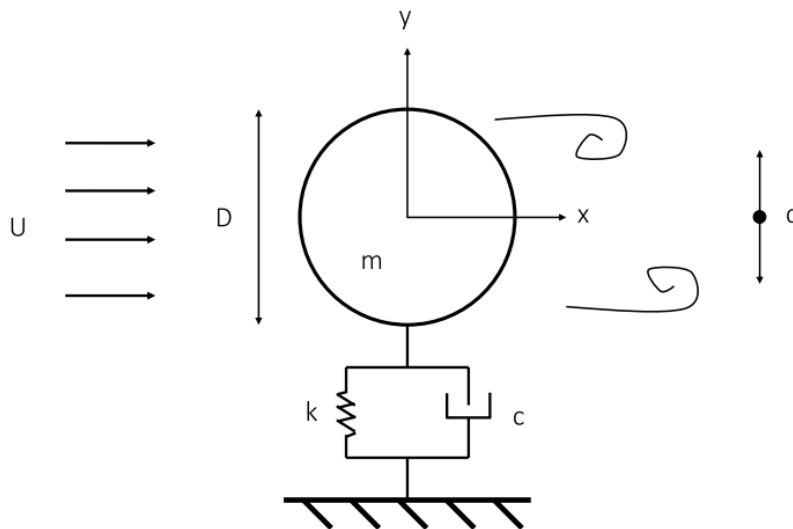**Image 9: Single-degree-of-freedom (1DOF) elastically mounted circular cylinder in uniform flow**

The structural equation governing this model is expressed as follows:

$$\ddot{y} + \left(4\pi\zeta f_N + \frac{2\pi f_{us}\gamma}{m^*}\right)\dot{y} + 4\pi^2 f_N^2 y = \frac{1}{4m} C_{L_o}\rho U^2 Dq \tag{2.3}$$

Where

$$\gamma = \frac{C_D}{4\pi St}, \qquad m^* = \frac{4m}{\pi\rho D^2 L} \quad and \quad q = \frac{2C_L}{C_{L_o}}$$

Where γ represents the stall parameter, f_N denotes the natural frequency, f_{us} the vortex shedding frequency, ζ represents the structural damping, m is the structural mass, C_{L_o} stands for the root-mean-square (RMS) lift acting on a stationary cylinder, q is the wake variable, C_L is the instantaneous lift coefficient, D is cylinder's diameter, m^* is the mass ratio.

Furthermore, the dynamically changing wake variable, q, is calculated according to the formula:

$$\ddot{q} + 2\pi f_{us}\varepsilon(q^2 - 1)\dot{q} + 4\pi^2 f_{us}^2 q = \beta Y \tag{2.4}$$

Where βY is a coupling parameter and ε is the damping parameter.

In its unforced state, the van der Pol oscillator exhibits a periodic response, gradually accumulating energy before rapidly discharging it. This phenomenon arises due to the influence of a non-linear damping term. The nonlinear damping effect is controlled by the damping parameter, ε, empirically determined within the VDP model.

2.3 Semi-Empirical Model by Pinheiro

Pinheiro's model in contrast with the models presented previously in this chapter, provides a framework for a three-dimensional mathematical model and introduces the concept of vortex cells to analyze fluid-structure interaction. Image 10 illustrates an example of a tower structure analyzed within this model. [3]
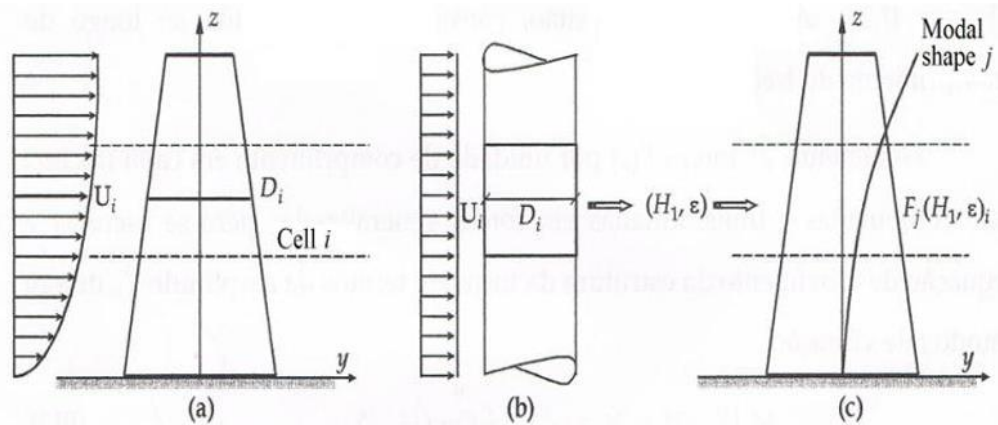

Image 10: Illustration outlining Pinheiro's model for analyzing the phenomenon of VIV in thin structures: (a) Depiction of vortex cells within the structure (b) Representation of laminar flow around a constant circular section (c) Aeroelastic modal force F_j

Each segment of the structure is characterized by its unique diameter D_i and average wind velocity U_i, which is associated with specific shedding frequencies f_i. These parameters are linked through the section's Strouhal number as expressed by Equation (2.5).

$$S = \frac{f_i D_i}{U_i}$$

(2.5)

In Pinheiro's model, the aeroelastic force acting on each section is determined by Scanlan's two-dimensional model, as detailed in Chapter 3.1. The structure is subjected to laminar wind speed as depicted in Image 10 (b). The motion equation governing the behavior of the tower structure is expressed as follows:

$$M_j(\ddot{Y}_j + 2\xi_j\omega_j\dot{Y}_j + \omega_j^2 Y_j) = Fm_j(H_1, \varepsilon)$$

(2.6)

Where M_j represents the structure's mass, Y_j is the amplitude corresponding to the jth natural vibration mode, ω_j and ξ_j denote the natural frequency and damping at jth mode and F_{mj} signifies the modal force.

The application of the model extends to cantilevered towers by integrating the modal shape. Simplifying the analysis, it is assumed that the vortex shedding occurs in a single frequency. Consequently, the entire tower is treated as a single vortex cell as shown in Image 11.
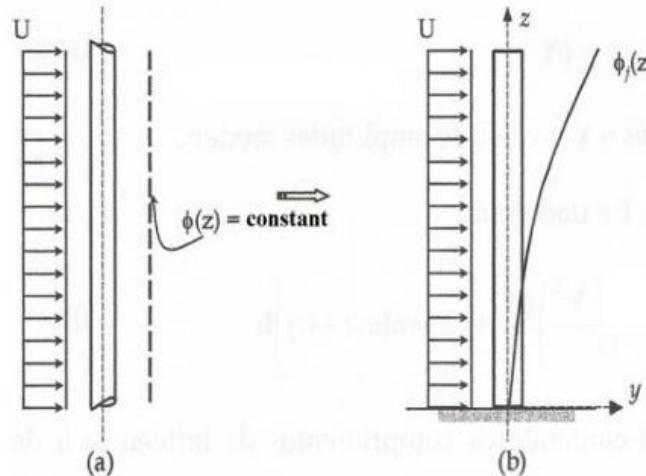
Image 11: Incorporating of modal shape and corresponding discretization

In the subsequent chapters, a deeper analysis of vortex-induced vibrations (VIV) will be undertaken, focusing on three single-degree-of-freedom (1DOF) models and one two-degree-of-freedom model (2DOF) model. Specifically, the R. H. Scanlan model, the Vickery

and Basu nonlinear model, the Basu and Vickery linear model, and the Hartlen-Currie model will be explored. Each of these models offers a unique insight and approach to understanding the VIV phenomenon in engineering structures. There will be a detailed examination of their theoretical foundations and mathematical formulations.

3. Single-Degree-of-Freedom Models used for VIV Analysis

It's important to note that the single-degree-of-freedom models that will be presented are specifically tailored to calculate amplitudes within the lock-in region.

3.1 R. H. Scanlan Model

Scanlan's single-degree-of-freedom (1DOF) empirical nonlinear model stands as a renowned engineering model for analyzing the phenomenon of Vortex-Induced Vibrations (VIV). At its core, the model is represented by a dynamic equation encapsulating the motion of the system under the influence of vortex-induced forces. Specifically, the equation describes the dynamics of the system, accounting for mass, m, damping, ζ, natural frequency, ω_1, and various aerodynamic parameters such as H_1, H_2, ε and C_L. [3] The model gains its nonlinearity by incorporating a nonlinear aerodynamic cubic term, resulting in the following equation:

$$m[\ddot{y} + 2\zeta\omega_1\dot{y} + \omega_1^2 y] = \frac{1}{2}\rho U^2 D\left[H_1\left(1 - \varepsilon\frac{y^2}{D^2}\right)\frac{\dot{y}}{U} + H_2\frac{y}{D} + \frac{1}{2}C_L\sin(\omega t + \alpha)\right] \quad (3.1)$$

Where H_1 is an experimentally obtained adjustment parameter related to linear aerodynamic damping, H_2 is an experimentally obtained adjustment parameter related to the aerodynamic stiffness, ε is an experimentally obtained non-linear aerodynamic damping parameter and a is an experimentally obtained adjustment parameter that represents the phase difference between the vortex shedding and displacement response. [21] Additionally, m is considered the cylinder's mass, ω_1 denotes the natural frequency, ρ refers to air density ($\rho = 1.225 \ kg/m^3$), D stands for the cylinder's diameter, U indicates wind velocity and ω signifies the vortex-shedding frequency complying with the Strouhal relation, $St = fD/U$, where St denotes the Strouhal number. [22]

The parameters H_1 and ε are derived from experimental data, specifically by observing two resonance response amplitudes, A_{y_1} and A_{y_2}, corresponding to two distinct damping values, ζ_1, and ζ_2.

$$H_1 = \frac{8m\pi S_t\left(\zeta_2 A_{y_1}^2 - \zeta_1 A_{y_2}^2\right)}{D^2\rho\left(A_{y_1}^2 - A_{y_2}^2\right)} \quad (3.2)$$

$$\varepsilon = \frac{4(\zeta_1 - \zeta_2)D^2}{\zeta_1 A_{y_2}^2 - \zeta_2 A_{y_1}^2} \quad (3.3)$$

The resonance response amplitudes are calculated from the equation:

$$A_{y_n} = 0.07\gamma \frac{\sqrt{0.3 + \dfrac{0.72}{(1.9 + \delta_r) \cdot S}}}{(1.9 + \delta_r) \cdot S^2} D \qquad (3.4)$$

Where

$$\delta_r = \frac{4m\pi\zeta_n}{\rho D^2} \ and \ \gamma: geometrical \ parameter \qquad (3.5)$$

The lock-in range is set to span within a 20% range around the area where the critical shedding frequency is met. Beyond this range, the cylinder experiences slight displacements which are induced by the force described below:

$$F = \frac{1}{2}\rho U^2 D C_L \sin(\omega_s t + a) \qquad (3.6)$$

Where

$$\omega_s = 2\pi f_s = 2\pi \frac{SU}{D}$$

In lock-in phenomena, the contributions of C_L and H_2 can be disregarded due to their relatively small magnitudes compared to the aerodynamic damping parameter. As a result, the Equation (3.1) is modified as follows [3]:

$$m[\ddot{y} + 2\zeta\omega_1\dot{y} + \omega_1^2 y] = \underbrace{\frac{1}{2}\rho U^2 D \left[H_1\left(1 - \varepsilon\frac{y^2}{D^2}\right)\frac{\dot{y}}{U}\right]}_{F(y,\dot{y})} \qquad (3.7)$$

For the numerical solution of the nonlinear equation, we proceed with its linearization through the application of Taylor's expansion on the nonlinear terms. The derivatives of the $F(y,\dot{y})$ are evaluated at the reference point y_0, representing the equilibrium state of the structure. These derivatives are expressed as:

$$\left.\frac{\partial F}{\partial y}\right|_{\substack{y=y_0 \\ \dot{y}=\dot{y}_0}} = -\rho U H_1 \dot{y}_0 \varepsilon \frac{y_0}{D} \qquad (3.8)$$

$$\frac{\partial F}{\partial \dot{y}}\bigg|_{\substack{y=y_0 \\ \dot{y}=\dot{y}_0}} = \frac{1}{2}\rho UDH_1\left(1 - \varepsilon\frac{y_0^2}{D^2}\right)$$

(3.9)

The equation is linearized to this final form:

$$m\delta\ddot{y} + \left(c - \frac{\partial F}{\partial \dot{y}}\bigg|_{\substack{y=y_0 \\ \dot{y}=\dot{y}_0}}\right)\delta\dot{y} + \left(k - \frac{\partial F}{\partial y}\bigg|_{\substack{y=y_0 \\ \dot{y}=\dot{y}_0}}\right)\delta y$$
$$= F(y_0, \dot{y}_0) - m\ddot{y}_0 - c\dot{y}_0 - ky_0$$

(3.10)

Furthermore, the complete expressions for the model's parameters are provided as follows:

- Mass parameter: $M = m$

- Damping parameter: $C = c - \frac{\partial F}{\partial \dot{y}}\bigg|_{\substack{y=y_0 \\ \dot{y}=\dot{y}_0}} = 2m\zeta\omega_1 - \frac{1}{2}\rho UDH_1\left(1 - \varepsilon\frac{y_0^2}{D^2}\right)$

- Stiffness parameter: $K = k - \frac{\partial F}{\partial y}\bigg|_{\substack{y=y_0 \\ \dot{y}=\dot{y}_0}} = m\omega_1^2 + \rho UH_1\dot{y}_0\varepsilon\frac{y_0}{D}$

- Load parameter: $Q = F(y_0, \dot{y}_0) - m\ddot{y}_0 - c\dot{y}_0 - ky_0$

In this final linearized form, the model can now be solved using Newmark's method as detailed in Chapter 3.4.

3.2 Vickery and Basu Nonlinear Model

In addition to Scanlan's model discussed earlier, another notable 1DOF nonlinear model, proposed by Vickery and Basu, offers an alternative perspective on the system's response in the vortex-induced vibrations (VIV). Unlike, Scanlan's model, which incorporates nonlinearity in the displacement term $y(t)$, the Vickery and Basu model uniquely introduces nonlinearity in the velocity term, $\dot{y}(t)$.
The model's equation is as follows [16]:

$$\ddot{y}(t) - 2 \cdot \omega_n \frac{\rho d^2}{m_{eq}}\left[\left(K_a - \frac{Sc}{4\pi}\right) - K_a \cdot G \cdot \dot{y}(t)^2\right]\dot{y}(t) + \omega_n^2 \cdot y(t) = 0$$

(3.11)

Where ω_n signifies the system's natural frequency, ρ is air density ($\rho = 1.225 \ kg/m^3$), d represents the cylinder's diameter, K_a stands for the aerodynamic damping parameter for small oscillations (constant), G is a positive factor, Sc refers to the Scruton number and m_{eq} is the equivalent mass per unit length in kg/m.

The Scruton number denoted as Sc, functions as a single governing parameter that encapsulates structural mass and damping. It is calculated according to the following formula:

$$Sc = 4\pi \frac{m_{eq}\zeta_s}{\rho d^2} \tag{3.12}$$

For the numerical solution of the nonlinear equation, we proceed with its linearization through the application of Taylor's expansion on the nonlinear terms. The Equation (3.11) is linearized to this final form:

$$m_{eq}\delta\ddot{y} + (c + 6\omega_n\rho d^2 K_a G\dot{y}_0^2)\delta\dot{y} + k\delta y$$
$$= -m_{eq}\ddot{y}_0 - (c + 2\omega_n\rho d^2 K_a G\dot{y}_0^2)\dot{y}_0 - ky_0 \tag{3.13}$$

Where

$$c = 2\omega_n m_{eq}\zeta - 2\omega_n\rho d^2 K_a$$

$$k = \omega_n^2 m_{eq}$$

Furthermore, the complete expressions for the model's parameters are provided as follows:

- Mass parameter: $M = m_{eq}$

- Damping parameter: $C = 2\omega_n\left[m_{eq}\zeta - \rho d^2 K_a(1 - 3G\dot{y}_0^2)\right]$

- Stiffness parameter: $K = k$

- Load parameter: $Q = -m_{eq}\ddot{y}_0 - 2\omega_n\left[m_{eq}\zeta + \rho d^2 K_a(1 + G\dot{y}_0^2)\right]\dot{y}_0$
  $$- ky_0$$

In this final linearized form, the model can now be solved using Newmark's method as detailed in Chapter 3.4.

3.3 Basu and Vickery Linear Model

A common characteristic shared by the models proposed by Vickery and Basu, as well as Ehsan and Scanlan, is the assumption of the simultaneous existence of vortex-shedding lift and motion-induced force, with no correlation between the two forces. [16] However, the latter model primarily focuses on scenarios involving oscillations, where the motion-induced force dominates and the vortex-shedding load can be disregarded. In the context of self-excited and self-limited systems, energy transfer arises from negative damping rather than from the external forces. As a result, these systems are characterized as nonlinear. Presenting an alternative perspective, Vickery and Basu propose a linear model described by the following equation:

$$\ddot{y}(t) - 2 \cdot \omega_n \frac{\rho d^2}{m_{eq}} \left(\frac{Sc}{4\pi} - K_a \right) \dot{y}(t) + \omega_n^2 \cdot y(t) = \frac{F_L(t)}{M_n} \tag{3.14}$$

Where ω_n signifies the system's natural frequency, ρ is air density ($\rho = 1.225 \ kg/m^3$), d represents the cylinder's diameter, K_a stands for the aerodynamic damping parameter, Sc refers to the Scruton number, m_{eq} is the equivalent mass per unit length in kg/m, F_L is the vortex shedding force and M_n is the modal mass in kg in the nth mode of vibration.

In lock-in phenomena, the effect of the excitation force is negligible regarding the oscillations that occur.

The aerodynamic damping parameter, despite being utilized in a linear model, demonstrates instability due to its calculation method:

$$K_a = K_{a0} \left(1 - \left(\frac{\sigma_y}{a_L \cdot d} \right)^2 \right) \tag{3.15}$$

Where σ_y represents the standard deviation of the oscillation, a_L is a non-dimensional factor typically recommended to be 0.4 and d stands for the cylinder's diameter.

Even though the model proposed is linear, it conceals nonlinearity within the parameter K_a. This nonlinearity arises because K_a is calculated for each time period, resulting in its variation over time. The calculation of K_a involves using the standard deviation value, where $\sigma_y = \frac{A}{\sqrt{2}}$, with A being the amplitude of oscillation. The graphical representation of Equation (3.15), follows a parabolic law with negative curvature as σ_y/d increases.
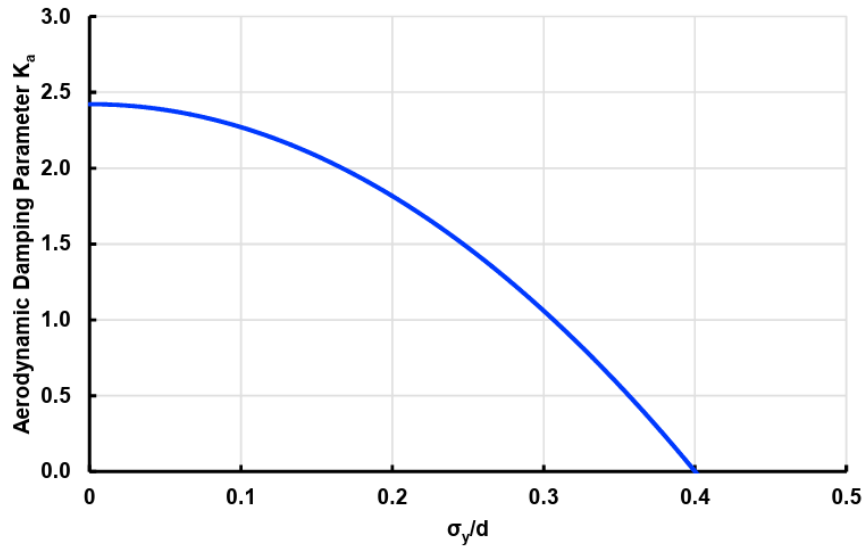
Image 12: Aerodynamic damping parameter K_a proposed by Vickery and Basu

$$(K_a = 2.422) \text{ and } \sigma_y/d = 0)$$

The Equation (3.14) is linearized to this final form:

$$m_{eq}\delta\ddot{y} + c\delta\dot{y} + k\delta y = -m_{eq}\ddot{y}_0 - c\dot{y}_0 - ky_0 \tag{3.16}$$

Where

$$c = 2\omega_n m_{eq}\zeta - 2\omega_n \rho d^2 K_a$$

$$k = \omega_n^2 m_{eq}$$

Furthermore, the complete expressions for the model's parameters are provided as follows:

- Mass parameter: $\quad M = m_{eq}$

- Damping parameter: $\quad C = c$

- Stiffness parameter: $\quad K = k$

- Load parameter: $\quad Q = -m_{eq}\ddot{y}_0 - c\dot{y}_0 - ky_0$

In this final linearized form, the model can now be solved using Newmark's method as detailed in Chapter 3.4.

The K_a-curve that is proposed underestimates the aeroelastic effect for small oscillations. As a result, a new model of the aerodynamic damping K_a is proposed and it is calculated according to the following equation [16]:

$$K_a = a \frac{e^{\left(-b\frac{\sigma_y}{d}\right)}}{\left(\frac{\sigma_y}{d}\right)^c} \quad with \ a, b, c > 0 \tag{3.17}$$

The curve-fitting process suggests the following values for the coefficients:

$$a = 0.3475, \qquad b = 5.808, \qquad c = 0.3582$$

This new model exhibits a distinct behavior characterized by positive curvature as shown in Image 13.
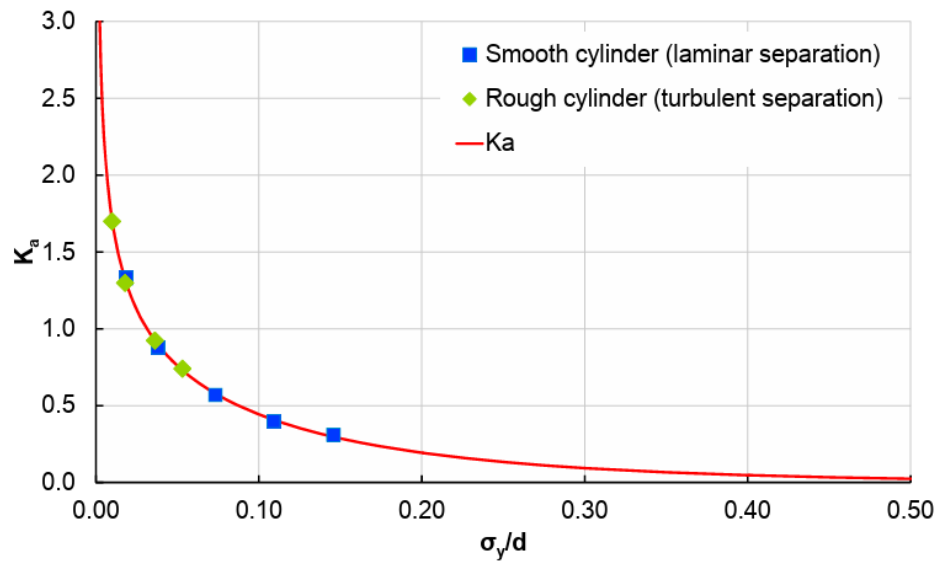

Image 13: Aerodynamic damping parameter K_a as a function of standard deviation for laminar and turbulent separation conditions ($Re = 2.6 \times 10^4$)

Comparing Image 12, which depicts the Vickery and Basu curve, with Image 13, it is evident that the new model demonstrates a steep decrease in aerodynamic damping for small oscillations, in contrast to the slow decrease observed in Image 12.

3.4 Newmark's Integration Method

Newmark's integration method offers a numerical basis for integrating the equations of motion in structural dynamics. [23] This method suggests that the system's future state, at the time t_{n+1}, is predicted based on the current state, at time t_n. Additionally, it introduces the parameters β and γ, which are crucial in determining the stability and accuracy of the method. The governing equation for the system's dynamic response can be expressed as:

$$M\delta\ddot{x}^n + C\delta\dot{x}^n + K\delta x^n = Q$$

(3.18)

Where δx represents the displacement, M is the mass, C is the damping, K is the stiffness and Q represents the external forces.

The Newmark's integration method, utilized to solve this equation, relies on a modified Taylor series expansion to approximate future states of the system. The approach breaks down the continuous dynamic response into discrete increments, allowing for the iterative calculation of displacements, velocities, and accelerations. After consideration and under Newmark's guidelines, the chosen values for the integration parameters in our computations are $\beta = 0.25$ and $\gamma = 0.5$. [24]

The system's acceleration $\delta\ddot{x}$ at a new time step based on the known values from the previous one, is calculated as follows:

$$x^n = x^{n-1} + \Delta t \cdot \dot{x}^{n-1} + \left(\frac{1}{2} - \beta\right)\Delta t^2 \cdot \ddot{x}^{n-1} + \beta\Delta t^2 \cdot \ddot{x}^n$$

$$\Rightarrow \boxed{\delta\ddot{x}^n = \frac{1}{\beta\Delta t^2}(x_0^n + \delta x^n - \tilde{x}^n) - \ddot{x}_0^n}$$

(3.19)

Where

$$\tilde{x}^n = x^{n-1} + \Delta t \cdot \dot{x}^{n-1} + \left(\frac{1}{2} - \beta\right)\Delta t^2 \cdot \ddot{x}^{n-1}$$

Similarly, the system's velocity $\delta\dot{x}$ at a new time step is calculated as:

$$\dot{x}^n = \dot{x}^{n-1} + (1 - \gamma)\Delta t \cdot \ddot{x}^{n-1} + \gamma\Delta t \cdot \ddot{x}^n$$

$$\Rightarrow \boxed{\delta\dot{x}^n = \tilde{x}^n + \frac{\gamma}{\beta\Delta t}(x_0^n + \delta x^n - \tilde{x}^n) - \dot{x}_0^n}$$

(3.20)

Where

$$\tilde{x}^n = \dot{x}^{n-1} + (1 - \gamma)\Delta t \cdot \ddot{x}^{n-1}$$

By substituting the calculated increments of displacement and velocity into the equation governing the system's dynamic response, it is possible to update the system's dynamics accurately. Hence, by applying these adjustments to Equation (3.18), we derive the following equation:

$$\left(\frac{M}{\beta \Delta t^2} + \frac{\gamma C}{\beta \Delta t} + K\right)\delta x^n = Q + \left(\frac{M}{\beta \Delta t^2} + \frac{\gamma C}{\beta \Delta t}\right)(\tilde{x}^n - x_0^n) - C\tilde{x}^n + M\ddot{x}_0^n + C\dot{x}_0^n \quad (3.21)$$

This equation leads to the calculation of the system's displacement δx by a linear algebraic system in the form of:

$$K_{eff} \cdot \delta x^n = Q_{eff}$$

$$\Rightarrow \boxed{\delta x^n = \frac{Q_{eff}}{K_{eff}}} \quad (3.22)$$

Where K_{eff} is the equivalent stiffness and Q_{eff} is the equivalent load.

The displacement, velocity, and acceleration values are calculated iteratively until the perturbations δx, $\delta \dot{x}$, and $\delta \ddot{x}$ are zeroed, according to the following formulas:

$$x = x + \delta x$$

$$\dot{x} = \dot{x} + \delta \dot{x}$$

$$\ddot{x} = \ddot{x} + \delta \dot{x}$$

When applying Newmark's integration method to solve 2DOF models, damping, stiffness, and load parameters are treated as matrices, and the variables representing the degrees of freedom are transformed into vectors.

3.5   Comparison of the single-degree-of-freedom models

System parameters were defined based on experimental data obtained from the literature. The selected values for these variables are summarized in Table 1. The results obtained from applying the models are compared against the theoretical predictions of Iwan Blevins's model in Image 8.

Table 1: Selected values for the 1DOF engineering models variables

Variable	Value
$\omega_n \ (rad/sec)$	125.66
$f \ (Hz)$	20
$D \ (m)$	0.05
$\rho_{wind} \ (kg/m^3)$	1.225
$m \ (kg)$	0.5958
$U \ (m/s)$	5.4
$f_s \ (Hz)$	21.6
$\omega_s \ (rad/sec)$	135.72
f_s/f	1.08

The first model, R. H. Scanlan's model, also includes parameters such as the geometrical parameter γ, extracted from Image 8 as the value mentioned for a simple support beam. Furthermore, the reduced damping parameter, δ_r needs to be defined and it is calculated according to Equation (3.5). The value of variable γ is presented in Table 2. The model was tested for two different cases.

Table 2: Selected value for the R. H. Scanlan model variable

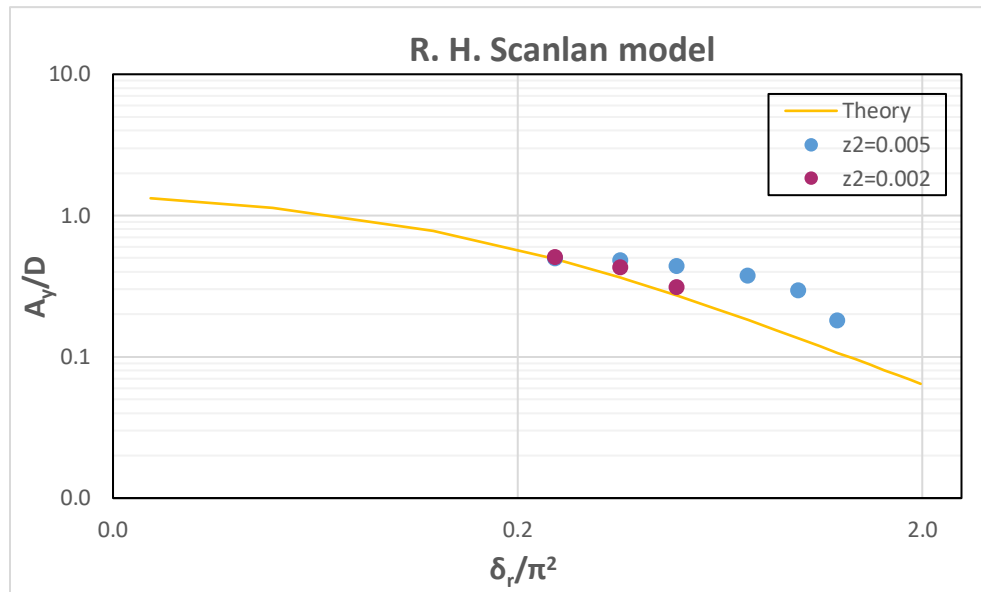| Variable	Value
γ	1.155

Figure 1: Comparison of R. H. Scanlan model results with Iwan Blevins theoretical predictions

Following the plot illustrating the model's results, there is a presentation of the according values in the tables down below.

Table 3: 1st case of R. H. Scanlan model results

$\zeta_1 = 0.001 \ and \ \zeta_2 = 0.005$			
ζ	δ_r/π^2	$A_{y(predicted)}$	A_y/D
0.00100	0.248	0.0248	0.496
0.00145	0.359	0.0240	0.480
0.00200	0.495	0.0220	0.440
0.00300	0.743	0.0188	0.376
0.00400	0.991	0.0147	0.294
0.00500	1.239	0.0090	0.180

Table 4: 2nd case of R. H. Scanlan model results

$\zeta_1 = 0.001 \ and \ \zeta_2 = 0.002$			
ζ	δ_r/π^2	$A_{y(predicted)}$	A_y/D
0.00100	0.248	0.0253	0.506
0.00145	0.359	0.0215	0.430
0.00200	0.495	0.0156	0.312

It is observed that the results corresponding to a smaller range of damping values (2nd case) demonstrate higher accuracy compared to the theoretical prediction.

Regarding the Vickery and Basu nonlinear model, the aerodynamic damping parameter, K_a, and the positive factor, G are essential parameters that determine the results. These parameters remain constant, and two distinct cases were examined. The resulting plot is depicted below:
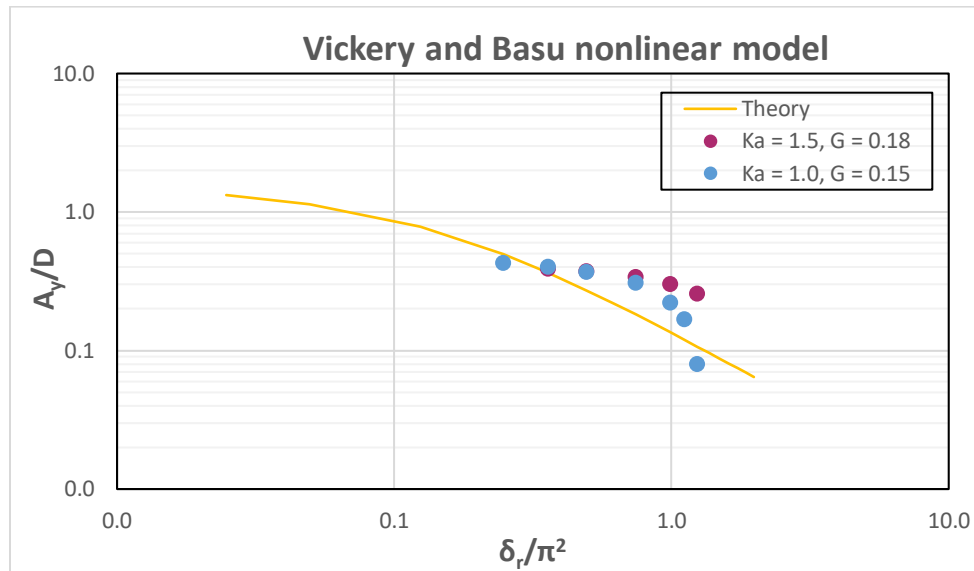

Figure 2: Comparison of Vickery and Basu nonlinear model results with Iwan Blevins theoretical predictions

Following the plot illustrating the model's results, there is a presentation of the according values in the tables down below.

Table 5: 1st case of Vickery and Basu nonlinear model results

$K_\alpha = 1.5 \; and \; G = 0.18$			
ζ	δ_r/π^2	$A_{y(predicted)}$	A_y/D
0.00145	0.359	0.0195	0.3900
0.00200	0.495	0.0186	0.3720
0.00300	0.743	0.0169	0.3380
0.00400	0.991	0.0150	0.3000
0.00500	1.2386	0.0128	0.2560

Table 6: 2nd case of Vickery and Basu nonlinear model results

ζ	δ_r/π^2	$A_{y(predicted)}$	A_y/D
	$K_\alpha = 1.0 \; and \; G = 0.15$		
0.00100	0.248	0.0213	0.4260
0.00145	0.359	0.0200	0.4000
0.00200	0.495	0.0185	0.3700
0.00300	0.743	0.0153	0.3060
0.00400	0.991	0.0111	0.2220
0.00450	1.1147	0.0084	0.1670
0.00500	1.2386	0.0040	0.0800

The comparison between Vickery and Basu's nonlinear model results and Iwan Blevins's theoretical predictions reveals significant insights into the behavior of the system. In the first case, where the aerodynamic damping parameter, K_a, is set to 1.5 and the positive factor G to 0.18, the amplitude of the structural displacement exhibits a gradual decrease with the increasing damping ratio, ζ. Similarly, in the second case, a similar trend is observed, albeit with different magnitudes of A_y. The behavior presented in both cases aligns with the anticipated damping effect of the VIV response.

The Basu and Vickery linear model incorporates the aerodynamic damping parameter, K_a, which is determined by the constant parameter, K_{a0}. Two distinct cases were examined based on variations in this constant parameter.

Table 7: 1st case of Basu and Vickery linear model results

ζ	δ_r/π^2	$A_{y(predicted)}$	A_y/D
	$K_{\alpha 0} = 2.42$		
0.00145	0.359	0.0195	0.3900
0.00200	0.495	0.0186	0.3720
0.00300	0.743	0.0169	0.3380
0.00400	0.991	0.0150	0.3000
0.00500	1.2386	0.0128	0.2560

Table 8: 2nd case of Basu and Vickery linear model results

$K_{\alpha 0} = 1.5$			
ζ	δ_r/π^2	$A_{y(predicted)}$	A_y/D
0.00100	0.248	0.0264	0.5280
0.00200	0.495	0.0243	0.4860
0.00300	0.743	0.0220	0.4400
0.00500	1.2386	0.0168	0.3360
0.00700	1.7340	0.0085	0.1700

To enhance the model's predictive accuracy, a new model of the aerodynamic damping, K_a, was tested, as outlined in Equation (3.17). In particular, the coefficient a was set to double the value proposed from the curve-fitting process, resulting in $a = 0.695$. The corresponding results are presented in Table 9.

Table 9: New model results

New model			
ζ	δ_r/π^2	$A_{y(predicted)}$	A_y/D
0.00100	0.248	0.0207	0.4140
0.00200	0.495	0.0141	0.2820
0.00300	0.743	0.0105	0.2100
0.00500	1.2386	0.0064	0.1280
0.00700	1.7340	0.0042	0.0840

Subsequently, the plot illustrating the model's results is presented in Figure 3.
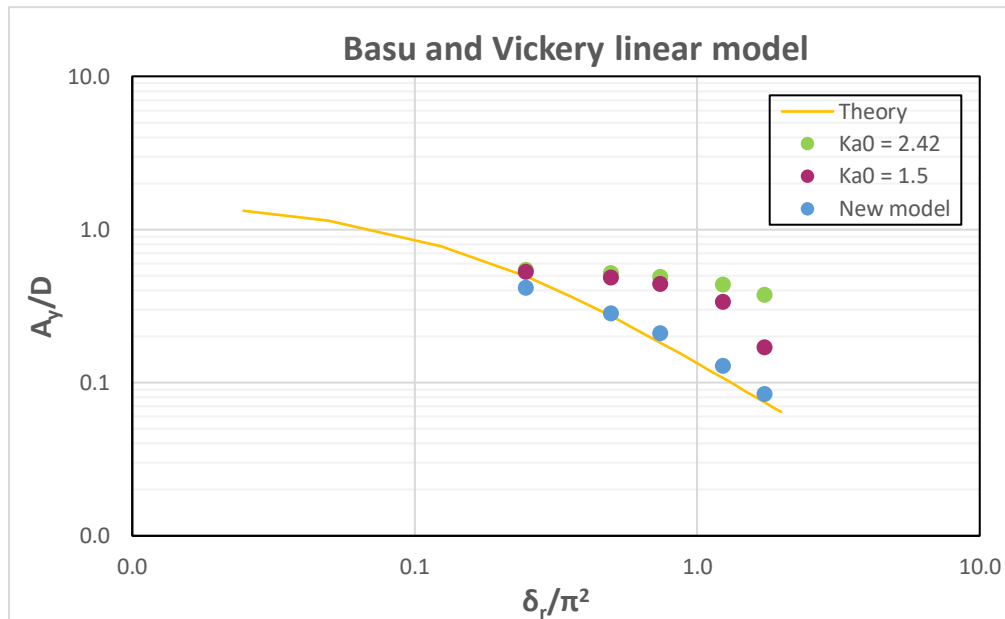
Figure 3: Comparison of Basu and Vickery linear model results with Iwan Blevins theoretical predictions

The comparison reveals that the new model aligns closely with the theoretical curve, indicating improved accuracy.

4. Two-Degrees-of-Freedom Hartlen-Curie Model

4.1 Equations and Framework of the Hartlen-Currie Model

This study introduces a comprehensive model by Hartlen and Currie aimed at capturing the dynamic behavior of an elastically mounted circular cylinder exposed to incoming wind. To focus our investigation on pure crosswind vibration, the circular cylinder is constrained to vibrate only in the crosswind direction.

The model comprises two primary components: a structural oscillator and an excitation oscillator, each tailored to encapsulate distinct phases of the system's dynamics. The structural oscillator, represented by the first equation of the model, describes the system as a second-order linear damped system. The excitation oscillator, characterized by the second equation, follows a similar format but with the lift coefficient serving as a secondary degree of freedom, offering deeper insights into the aerodynamic effects on the system dynamics.

The integration of the excitation oscillator with the structural oscillator is facilitated by a coupling term directly linked to the transverse velocity of the cylinder. This coupling allows their dynamic behaviors to interact closely, helping us understand how they both affect the overall system response. The model's equations are presented below [17]:

$$M\left(\ddot{Y} + 2\zeta\omega_n\dot{Y} + \omega_n^2 Y\right) = \frac{1}{2}\rho_\alpha U^2 LDC_L \tag{4.1}$$

$$\ddot{C}_L - G\left[C_{L_0} - \frac{4}{3}\left(\frac{\dot{C}_L}{\omega_s}\right)^2\right]\dot{C}_L + \omega_s^2 C_L = -H\dot{Y} \tag{4.2}$$

Where M is the cylinder's mass, Y is the displacement of the circular cylinder in the crosswind direction, ζ is the damping ratio, ω_n is the natural frequency of structure oscillator, ρ_α is air density, U is constant incoming wind velocity, L is the cylinder's length, D is the cylinder's diameter, ω_s is Strouhal frequency (proportional to wind velocity), C_{L_0} is the amplitude of C_L in the case there is no dynamic motion, and G and H are dimensionless parameters that play a crucial role in the model's dynamic response.

The Equations (4.1) and (4.2) are linearized as follows:

$$M\delta\ddot{Y} + c\delta\dot{Y} + k\delta Y - \frac{1}{2}\rho_\alpha U^2 LD\delta C_L = \frac{1}{2}\rho_\alpha U^2 LDC_L^0 - M\ddot{Y}_0 - c\dot{Y}_0 - kY_0 \qquad (4.3)$$

$$\delta\ddot{C}_L - G\left(C_{L_0} - \frac{4}{3}\cdot\frac{\dot{C}_L^{0^2}}{\omega_s^2}\right)\delta\dot{C}_L + \omega_s^2\delta C_L + H\delta\dot{Y} = -H\dot{Y}_0 - \ddot{C}_L^0$$

$$+G\left(C_{L_0} - \frac{4}{3}\cdot\frac{\dot{C}_L^{0^2}}{\omega_s^2}\right)\dot{C}_L^0 - \omega_s^2 C_L^0 \quad (4.4)$$

Where $c = 2M\zeta\omega_n$ and $k = M\omega_n^2$

As a consequence, the matrices that emerge are presented below:

- Mass matrix: $M' = \begin{bmatrix} M & 0 \\ 0 & 1 \end{bmatrix}$

- Damping matrix: $C = \begin{bmatrix} c & 0 \\ H & -G\left(C_{L_0} - \dfrac{4\cdot\dot{C}_L^{0^2}}{\omega_s^2}\right) \end{bmatrix}$

- Stiffness matrix: $K = \begin{bmatrix} k & -\dfrac{1}{2}\rho_\alpha U^2 LD \\ 0 & \omega_s^2 \end{bmatrix}$

- Load matrix: $Q = \begin{bmatrix} \dfrac{1}{2}\rho_\alpha U^2 LDC_L^0 - M\ddot{Y}_0 - c\dot{Y}_0 - kY_0 \\ -H\dot{Y}_0 - \ddot{C}_L^0 + G\left(C_{L_0} - \dfrac{4}{3}\cdot\dfrac{\dot{C}_L^{0^2}}{\omega_s^2}\right)\dot{C}_L^0 - \omega_s^2 C_L^0 \end{bmatrix}$

The final equation in the form of matrices is:

$$M'\begin{Bmatrix} \delta\ddot{y} \\ \delta\ddot{C}_L \end{Bmatrix} + C\begin{Bmatrix} \delta\dot{y} \\ \delta\dot{C}_L \end{Bmatrix} + K\begin{Bmatrix} \delta y \\ \delta C_L \end{Bmatrix} = Q \qquad (4.5)$$

Another modified version of the same model utilizes the dimensionless parameters G' and F. Their formula based on the parameters G and H is as follows:

$$G = G' \cdot \omega_s \Rightarrow \boxed{G' = \frac{G}{\omega_s}} \tag{4.6}$$

$$H = \frac{F \cdot \omega_s}{D} \Rightarrow \boxed{F = \frac{H \cdot D}{\omega_s}} \tag{4.7}$$

The modified equations of the model become:

$$M\left(\ddot{Y} + 2\zeta\omega_n\dot{Y} + \omega_n^2 Y\right) = \frac{1}{2}\rho_\alpha U^2 L D C_L \tag{4.8}$$

$$\ddot{C}_L - \frac{G'}{\omega_s}\left[C_{L_0} - \frac{4}{3}\left(\frac{\dot{C}_L}{\omega_s}\right)^2\right]\dot{C}_L + \omega_s^2 C_L = -\frac{F \cdot \omega_s}{D}\dot{Y} \tag{4.9}$$

The actual difference from the previous version of the model lies in the damping and the load matrix, which are transformed as follows:

- Damping matrix:

$$C = \begin{bmatrix} c & 0 \\ \dfrac{F \cdot \omega_s}{D} & -G' \cdot \omega_s\left(C_{L_0} - \dfrac{4 \cdot \dot{C}_L^{0^2}}{\omega_s^2}\right) \end{bmatrix}$$

- Load matrix:

$$Q = \begin{bmatrix} \dfrac{1}{2}\rho_\alpha U^2 L D C_L^0 - M\ddot{Y}_0 - c\dot{Y}_0 - kY_0 \\ -\dfrac{F \cdot \omega_s}{D}\dot{Y}_0 - \ddot{C}_L^0 + G' \cdot \omega_s\left(C_{L_0} - \dfrac{4}{3}\cdot\dfrac{\dot{C}_L^{0^2}}{\omega_s^2}\right)\dot{C}_L^0 - \omega_s^2 C_L^0 \end{bmatrix}$$

In this final linearized form, the model can now be solved using Newmark's method as detailed in Chapter 3.4.

G' and F are non-dimensional with respect to ω_s and D. That means that constant G' and F values provide the same A/D for the same ω_s/ω_n.

The results derived from the Hartlen-Curie two-degrees-of-freedom model (2DOF Model) are compared against the experimental observations reported by Feng, as illustrated in Image 14. [25]
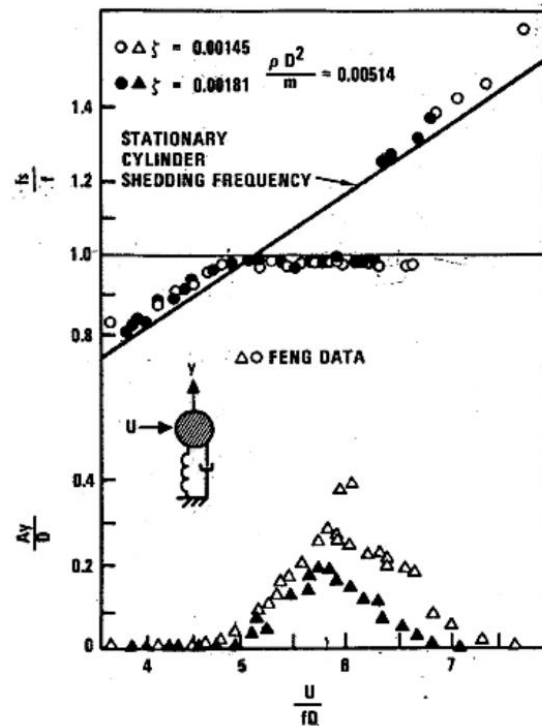
Image 14: Vortex-induced vibration of a damped circular cylinder

Notably, this plot highlights a sudden increase in oscillation amplitude occurring within the range $U/fD = 5 \div 7$, coinciding with the equality of shedding and natural frequency. This phenomenon signifies the lock-in phenomenon, where the cylinder's oscillation frequency becomes synchronized with the shedding frequency of vortices. [17] The comparison is further elucidated by observing the diagonal line in the plot, which represents a stationary cylinder shedding frequency, thereby indicating a constant Strouhal number ($St = 0.2$) across varying flow velocities. [26] This constant Strouhal number is a critical reference for understanding the relationship between shedding frequency and flow velocity. The inclusion of this comparative analysis not only tests the validity of the Hartlen-Curie model but also contributes to the broader understanding of the VIV phenomenon.

4.2   Optimization Procedure for Model Parameter Determination

To determine the parameters G and H of the engineering model, two distinct optimization methods are applied. The aim is to iteratively define the values of these parameters to achieve a desired targeted outcome. Consequently, an objective function F_{aim} was formulated following the subsequent procedure.

Initially, a natural frequency value, ω_n, was selected. Subsequently, a diameter value was chosen, enabling the determination of mass using the equation from Image 14:

$$\frac{\rho D^2}{m} = 0.00514 \Rightarrow m = \frac{\rho D^2}{0.00514} \tag{4.10}$$

Where $\rho \equiv \rho_{wind}$

Following this, the cylinder's length and damping value were determined. A wind velocity value was then selected to calculate the corresponding Reynolds number:

$$Re = \frac{Ud}{nu} \tag{4.11}$$

Utilizing data from the flow simulations around a circular cylinder (Image 15), the amplitude of C_L, denoted as C_{L_0}, was established. [27]
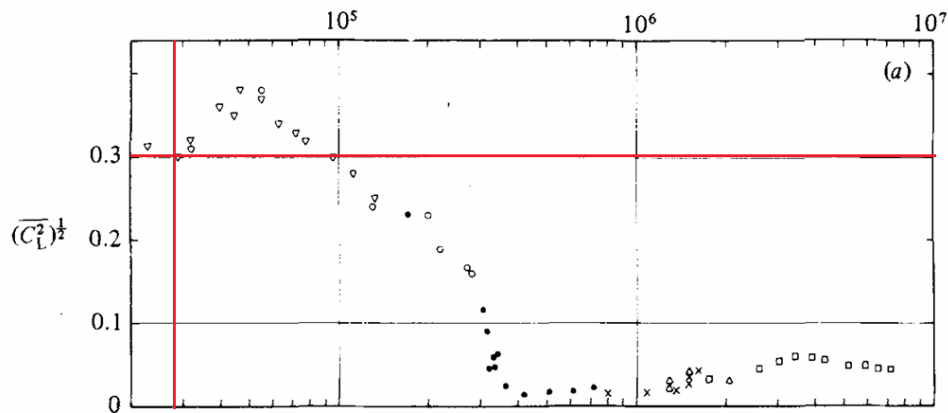
Image 15: Data from flow simulations around a circular cylinder, depicting the relationship between Reynolds number (Re) and the lift coefficient (C_L)

Additionally, by selecting Strouhal's number value to be the one for a rigid cylinder, the shedding frequency was calculated using the following equations:

$$St = \frac{f_s \cdot D}{U} \Rightarrow f_s = \frac{St \cdot U}{D} \Rightarrow \omega_s = 2\pi f_s \tag{4.12}$$

Subsequently, referring again to Image 14, the value of the anticipated maximum displacement A is defined from the value of the y-axis, A_y/d.

As a result, the targeted equation can be formulated as:

$$y_{targ} = A\cos(\omega_n t)$$

(4.13)

Where $A \equiv A_y \equiv A_{target}$

The objective function is then given by Equation (4.14).

$$F_{aim} = \left(A - A_{target}\right)^2$$

(4.14)

The same objective function ($F_{aim} \equiv F$) is used for the optimization methods analyzed in the following chapters.

The specific values selected for the various variables involved in the engineering model are included in Table 10:

Table 10: Selected values for the Hartlen-Currie model variables

Variable	Value
$\omega_n \ (rad/sec)$	20
$f \ (Hz)$	3.18
$D \ (m)$	0.15
$\rho_{wind} \ (kg/m^3)$	1.225
$m \ (kg)$	5.36
$L \ (m)$	1.8
ζ	0.00181
$U \ (m/s)$	2.6
$nu \ (m^2/s)$	1.5×10^{-5}
Re	26000
C_{L_0}	0.3
St	0.2
$f_s \ (Hz)$	3.47
$\omega_s \ (rad/sec)$	21.78
f_s/f	1.09
A_y/D	0.15
$A_{target} \ (m)$	0.0225

4.2.1   COBYLA Optimization Method

COBYLA, an acronym for Constrained Optimization by Linear Approximation, offers a reliable method for constrained optimization. This method relies on linear approximations of both the objective function and each constraint, offering a practical guide for solving optimization problems. Implemented in Fortran, COBYLA is based on a nonlinear derivative-free constrained optimization, utilizing a linear approximation. [28]

At each iteration, COBYLA maintains a set of points, an approximate solution, and a radius parameter. This set of points represents potential solutions. The algorithm constructs linear approximations to the objective function and constraint functions based on these points, ensuring that their values agree with the linear approximation. These linear approximations are then used to formulate a linear program, where the objective is to minimize the function subject to the constraints. The solution must remain within a specified radius from the current point. Throughout the optimization process, the radius parameter gradually decreases, facilitating convergence towards the optimal solution.

In applying the COBYLA optimization method to the problem, Python's **'fmin_cobyla'** function from the 'scipy.optimize' module in the SciPy library was utilized. By incorporating this function into the workflow, optimal values for the parameters G and H were determined, effectively minimizing the objective function and enhancing the performance of the engineering model.

The function call follows the syntax [29]:

$$scipy.optimize.fmin\_cobyla(func, x0, [constraints], rhoend)$$

Where $func$ is the objective function to minimize, $x0$ denotes the initial guess for the parameter values, [constraints] encompasses any constraints imposed on the optimization problem (in this case, none) and $rhoend$ specifies the final accuracy desired in the optimization process, although precise guarantee of this accuracy is not ensured (in this case, $rhoend = 10^{-5}$).

4.2.2   Newton Optimization Method

Newton's Method is a widely used optimization technique that aims to find the minimum of a given objective function by iteratively updating the parameters based on the function's gradients and second derivatives. The method is characterized by its rapid convergence, especially when the initial guess is close to the optimal solution. [30]

The method involves computing the first and second derivatives of the objective function and utilizing them to update the parameters in a way that minimizes the function. The equation used for the iterations consists of the Hessian matrix, which is often denoted as H or $\nabla^2 f$ and is a square matrix of second-order partial derivatives. Its size is $n \times n$, where n is the number of variables. The iterations are made according to the following update formula:

$$\begin{Bmatrix} G \\ H \end{Bmatrix}^{k+1} = \begin{Bmatrix} G \\ H \end{Bmatrix}^{k} - \eta \underbrace{\begin{bmatrix} \dfrac{\partial^2 F}{\partial G^2} & \dfrac{\partial^2 F}{\partial G \partial H} \\ \dfrac{\partial^2 F}{\partial G \partial H} & \dfrac{\partial^2 F}{\partial H^2} \end{bmatrix}^{-1}}_{Hessian\ matrix} \begin{Bmatrix} \dfrac{\partial F}{\partial G} \\ \dfrac{\partial F}{\partial H} \end{Bmatrix} \tag{4.15}$$

Where η denotes a single, numerical value without any additional directional information (in this case, $\eta = 1$), F is the objective function, and G and H are the parameters being optimized. [31]

First-order derivatives are calculated as follows:

$$\frac{\partial F}{\partial G} = \frac{F(G^k + \delta G, H^k) - F(G^k - \delta G, H^k)}{2\delta G} \tag{4.16}$$

$$\frac{\partial F}{\partial H} = \frac{F(G^k, H^k + \delta H) - F(G^k, H^k - \delta H)}{2\delta H} \tag{4.17}$$

Second-order derivatives are calculated as follows:

$$\frac{\partial^2 F}{\partial G \partial H} = \frac{F(G^k + \delta G, H^k + \delta H) - F(G^k + \delta G, H^k - \delta H)}{4\delta G \delta H}$$
$$+ \frac{F(G^k - \delta G, H^k - \delta H) - F(G^k - \delta G, H^k + \delta H)}{4\delta G \delta H} \tag{4.18}$$

$$\frac{\partial^2 F}{\partial G^2} = \frac{F(G^k + \delta G, H^k) - 2F(G^k, H^k) + F(G^k - \delta G, H^k)}{\delta G^2} \tag{4.19}$$

$$\frac{\partial^2 F}{\partial H^2} = \frac{F(G^k, H^k + \delta H) - 2F(G^k, H^k) + F(G^k, H^k - \delta H)}{\delta H^2} \tag{4.20}$$

4.2.3   Comparison of Optimization Methods

Following Table 10, the expected A_{target} value is $0.225\,m$. Utilizing both optimization methods, the following plots were obtained illustrating the results for each method. To begin with, the outcomes obtained using the Newton Method:
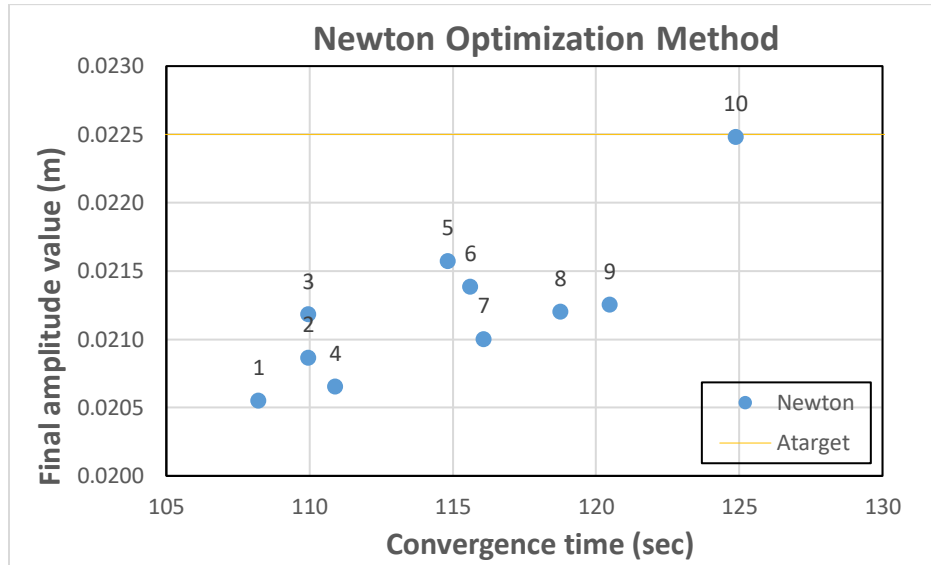
Figure 4: Optimization results using the Newton method

The optimization process involved applying the Newton method to different sets of original values G and H. It was observed that multiple sets of parameters met the criteria of approaching or achieving the exact A_{target}, with minimum or no divergence from the convergence criteria ($F_{aim} = 0$). The resulting values, also depicted in the plot above, are summarized in Table 11. It is worth mentioning that the values of G and H are of the same order.

Table 11: Summary of Newton optimization results

	G	H	F_{aim}	Convergence Time (sec)	$A\ (m)$
1	86.3	82.0	4×10^{-6}	108.2	0.0206
2	86.5	80.0	3×10^{-6}	110.0	0.0209
3	86.9	90.0	2×10^{-6}	110.0	0.0212
4	86.2	70.0	3×10^{-6}	110.9	0.0207
5	86.9	74.0	9×10^{-7}	114.8	0.0216
6	86.6	65.0	1×10^{-6}	115.6	0.0214
7	86.1	52.4	2×10^{-6}	116.1	0.0210
8	86.1	45.8	2×10^{-6}	118.8	0.0212
9	86.0	40.0	2×10^{-6}	120.5	0.0213
10	86.9	50.0	4×10^{-10}	124.9	0.0225

Additionally, despite small deviations of the order of 10^{-4}, as F_{aim} is supposed to converge to a value of 10^{-10}, the convergence appears sufficiently rapid. Notably, the target frequency was expected to be $3.18\ Hz$, reflecting the structural natural frequency of the system and indicating the presence of a single dominant frequency in the lock-in range. However, it is observed that the actual dominant frequency value is approximately $3.21\ Hz$, indicating a slight deviation from the expected value.

The optimization process utilizing the COBYLA method began with the same initialization values for G and H as those used for the corresponding sets in the Newton method. Despite this shared starting point, the outcomes differ as shown in the plot below:
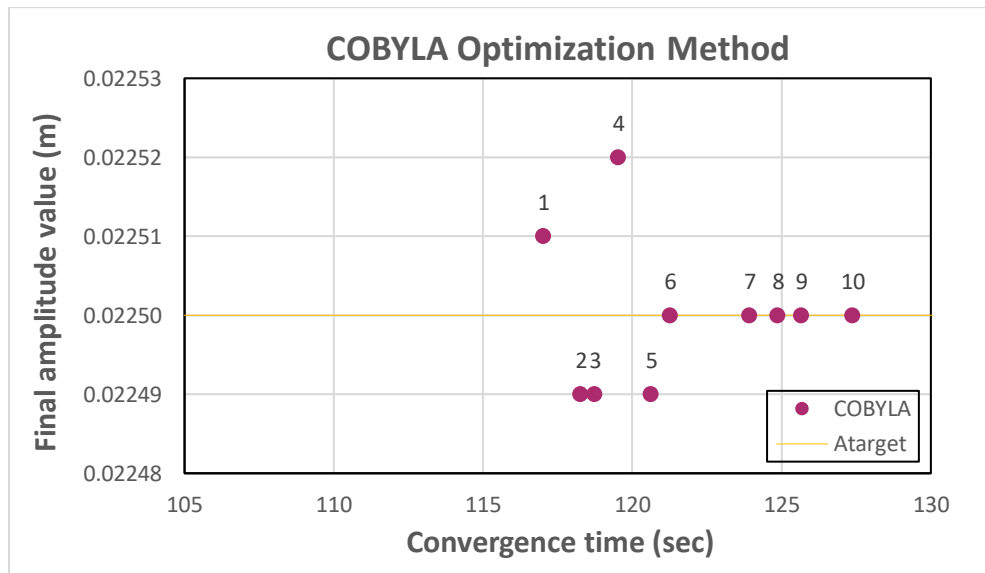
Figure 5: Optimization results using COBYLA method

Following the plot illustrating the optimization results, there is a presentation of the according values in Table 12.

Table 12: Summary of COBYLA optimization results

	G	H	F_{aim}	Convergence Time (sec)	$A\ (m)$
1	88.0	89.9	1×10^{-10}	117.0	0.02251
2	87.8	82.0	1×10^{-10}	118.3	0.02249
3	87.7	79.9	1×10^{-10}	118.8	0.02249
4	87.6	75.1	4×10^{-10}	119.5	0.02252
5	87.5	70.0	1×10^{-10}	120.6	0.02249
6	87.4	66.0	0	121.3	0.02250
7	87.0	53.5	0	123.9	0.02250
8	86.9	50.0	0	124.9	0.02250
9	86.8	46.8	0	125.7	0.02250
10	86.6	41.0	0	127.4	0.02250

Notably, similar to the results obtained with the Newton method, the values of G and H in the COBYLA optimization are of the same order showcasing a parallel behavior across the optimization techniques. Although several sets achieved near-perfect convergence with Faim, the dominant frequency value hovered around $3.21\ Hz$, slightly deviating from the anticipated $3.18\ Hz$. By presenting the results of both methods in the same plot, as shown in Figure 6, it becomes evident that while the Newton method tends to converge faster, the COBYLA method appears to offer greater precision in achieving the target amplitude, A_{target}. This observation prompts the decision to proceed with further analysis utilizing the COBYLA optimization method, ensuring more accurate estimations for the parameters G and H.
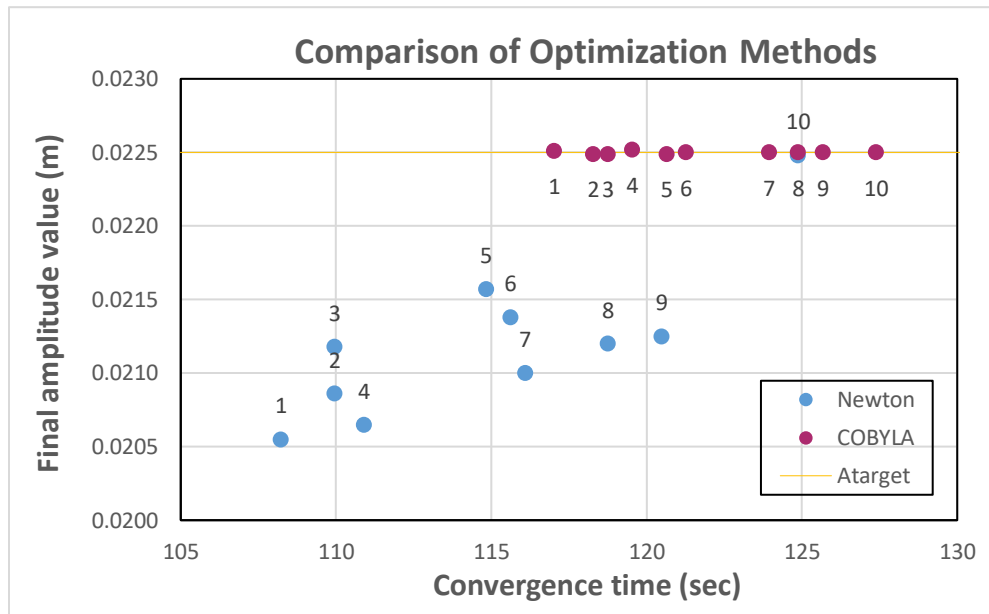
Figure 6: Comparison of optimization results between Newton and COBYLA methods

4.3   Exploring model behavior through iterative frequency ratio analysis

To examine the model's behavior, multiple cases of varying frequency ratios will be conducted, adjusting the dimensionless parameters accordingly. Table 13 outlines the values of the variables utilized in the Hartlen-Currie model for each case.

Table 13: Variables values for the Hartlen-Currie model

Variable	Value
D (m)	0.15
ρ_{wind} (kg/m^3)	1.225
m (kg)	5.4
L (m)	1.8
ζ	0.00181
nu (m^2/s)	1.5×10^{-5}
Re	26000
C_{L_0}	0.3
St	0.2

The procedural steps in each case involve identifying optimal values for the dimensionless parameters, G' and F, through the COBYLA optimization method. Subsequently, iterations are conducted using these parameters to determine the amplitude values across a range of flow velocities. The aim is to generate results that closely resemble the experimental Feng data depicted in Image 14.

4.3.1 Initiating frequency ratio analysis: Case f$_s$/f = 1.0

In the initial case, the natural frequency of the system is selected to match the shedding frequency. The anticipated maximum amplitude value of the oscillation was determined by identifying the maximum value from Image 14. Subsequently, this maximum value was set to be anticipated at a smaller value of U/fD than the actual U/fD value indicated in the image. This information is represented in Table 14, with the highlighted values indicating those specifically referenced.

Table 14: Selected values for the 1st case scenario

Variable	Value
ω_n (rad/sec)	20.0
f (Hz)	3.18
ω_s (rad/sec)	20.0
f_s (Hz)	3.18
f_s/f	1.0
U/fD	5.0
U (m/s)	2.39
A_y/D	0.2
A_{target} (m)	0.03

Following the application of the COBYLA optimization method, the dimensionless parameter values are presented in Table 15.

**Table 15: Dimensionless parameters values (1ˢᵗ case scenario)**

G	G'	H	F
45.43268	2.271634	100.192644	0.75144483

The optimal values result in the following depiction of the Hartlen-Currie model results. For these optimal values, the model produces the displacement shown below. It is observed that after approximately 110 seconds, the displacement fully converges to the targeted amplitude value. A zoomed-in plot of the same diagram reveals a minor divergence in the phase of the two curves.
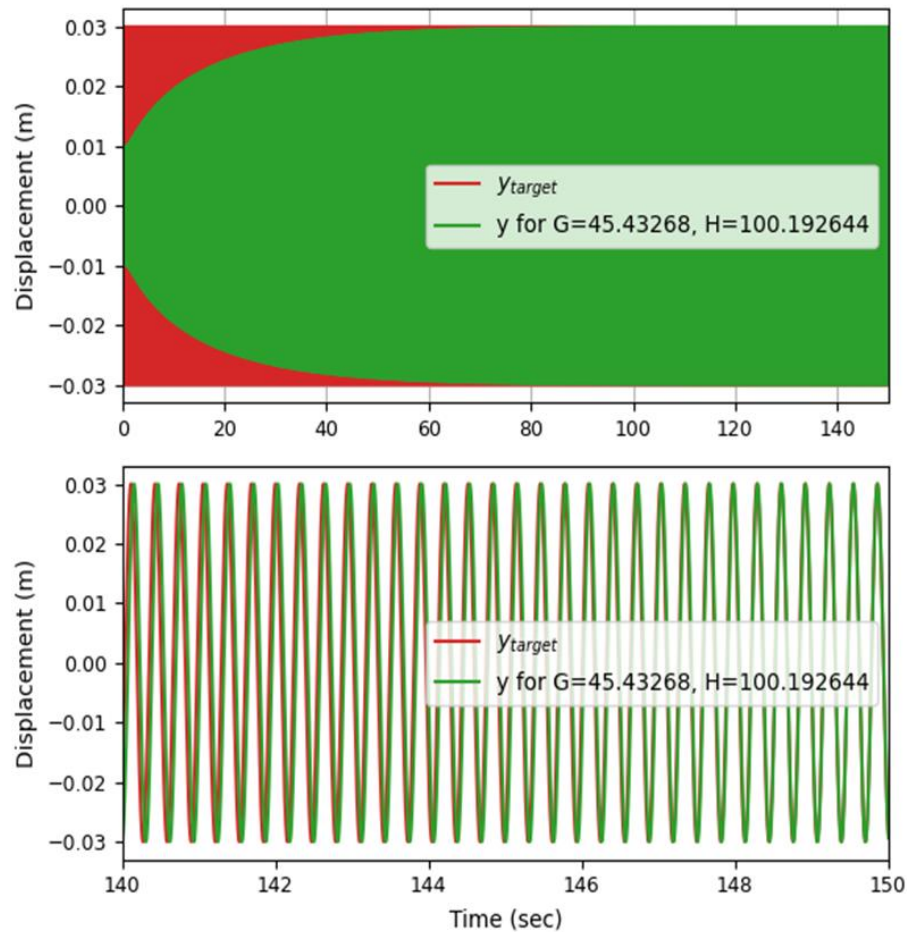
Figure 7: Displacement convergence over time according to the optimal dimensionless parameters values

The same pattern occurs in the other cases as well, ensuring that the optimal values are correctly calculated. To avoid repetition, these plots are not presented for the other cases.

The resultant plots are depicted in Figures 8 and 9.
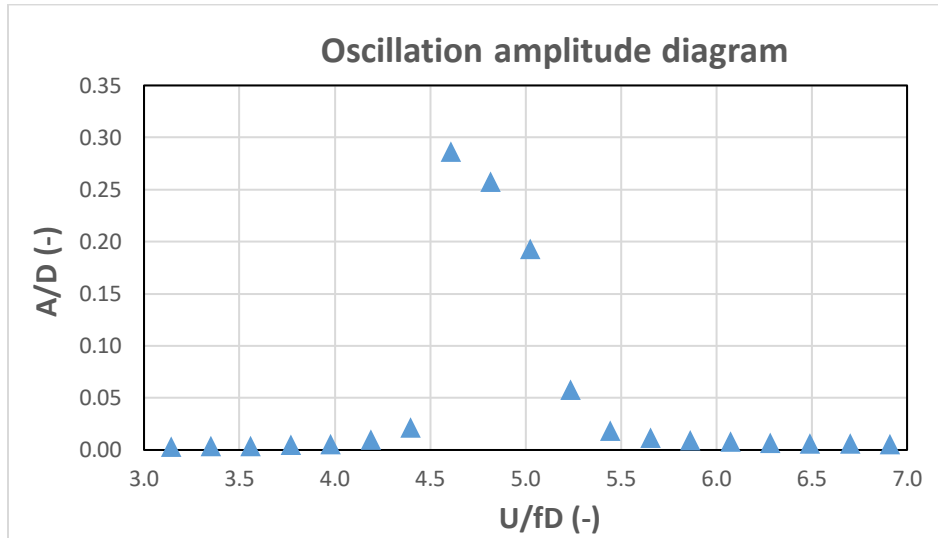
Figure 8: 1st case scenario oscillation amplitude diagram

It is observed that although the anticipated maximum A/D is 0.2 for $U/fD = 5.0$, the maximum value is $A/D = 0.285$ and occurs for $U/fD = 4.6$. Consequently, the maximum A/D is shifted slightly to the left and is not predicted as expected.
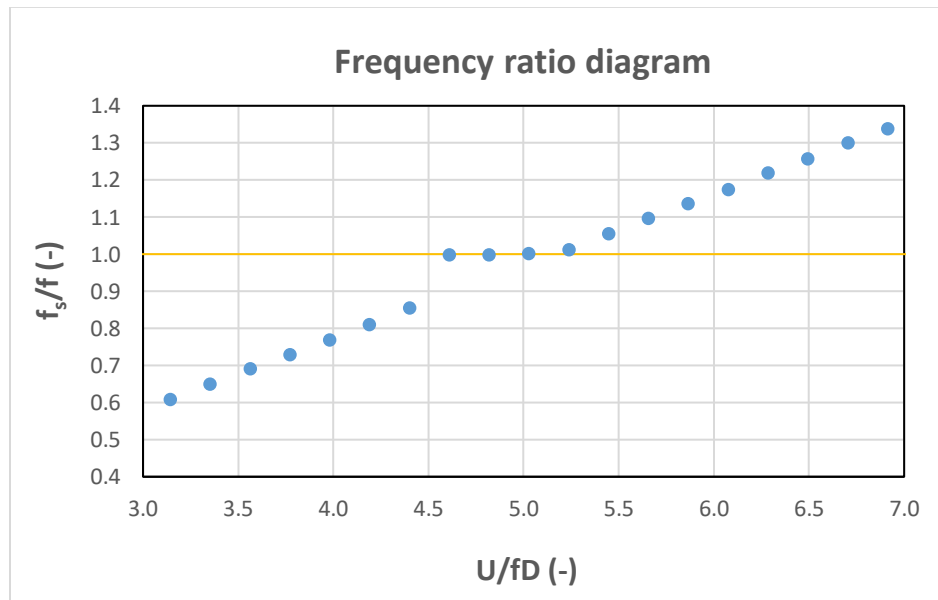
Figure 9: 1st case scenario frequency ratio diagram

The lock-in region is correctly predicted as the natural frequency is locked with the shedding frequency in the range of flow velocities where the maximum amplitudes are produced. However, there is a slight shift of the frequency ratio values to the left in this region.

4.3.2   Continuing frequency ratio analysis: Case f_s/f = 1.16

In this case, the goal is to predict the exact result from Image 14. To achieve this, the maximum amplitude value is determined according to the maximum A/D depicted in the image, and then the corresponding value for the U/fD is set. The natural frequency of the system remains the same as the one in the previous case, and the shedding frequency is determined from the Strouhal number equation (Equation 4.12) which is proportional to the flow velocity. This information is presented in Table 16.

Table 16: Selected values for the 2nd case scenario

Variable	Value
$\omega_n \ (rad/sec)$	20.0
$f \ (Hz)$	3.18
$\omega_s \ (rad/sec)$	23.2
$f_s \ (Hz)$	3.69
f_s/f	1.16
U/fD	5.8
$U \ (m/s)$	2.77
A_y/D	0.2
$A_{target} \ (m)$	0.03

Following the application of the COBYLA optimization method, the dimensionless parameter values are presented in Table 17.

Table 17: Dimensionless parameters values (2nd case scenario)

G	G'	H	F
132.275528	5.701531379	79.855139	0.516304778

As the slight shift in the maximum amplitude values is observed again, another correction procedure is implemented. Within the lock-in region, the maximum amplitude values are determined through separate optimization procedures. Specifically, each value is obtained by conducting an optimization procedure with the COBYLA method to identify the appropriate parameters that will align with the actual anticipated values. The parameters that occurred for three separate points in the lock-in region are presented in Table 18.

Table 18: Dimensionless parameters values (2nd case scenario)

U/fD	G	G'	H	F
5.45	94.074227	4.315331514	79.873155	0.549585929
5.7	121.014418	5.307649912	79.87445	0.525489803
5.78	127.992689	5.53601596	81.125149	0.526330984

The corrected values of G' and F are presented in Figure 10.
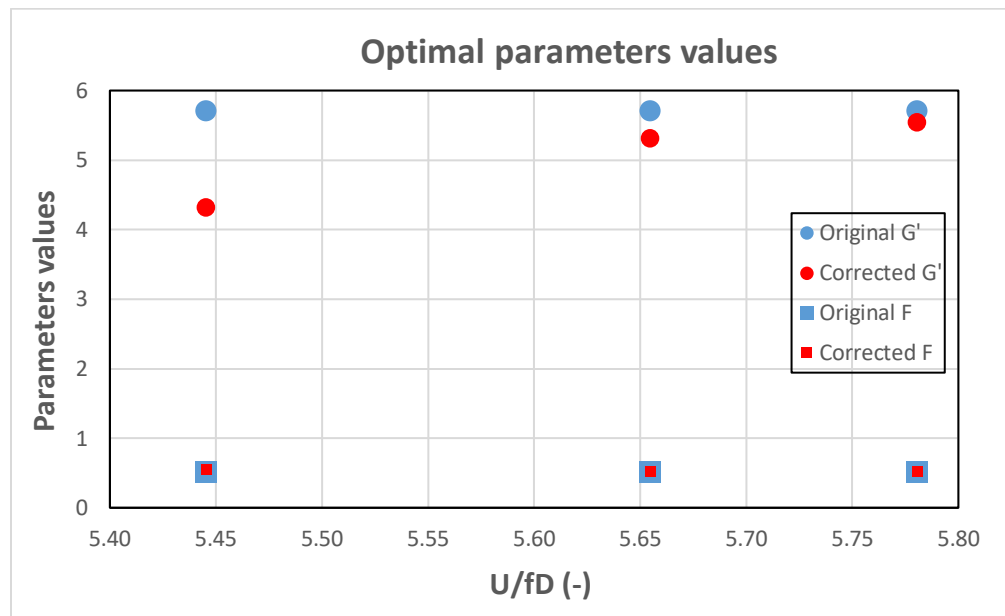
Figure 10: Corrected parameters values (2nd case)

The resultant plots are depicted below in Figures 11 and 12.
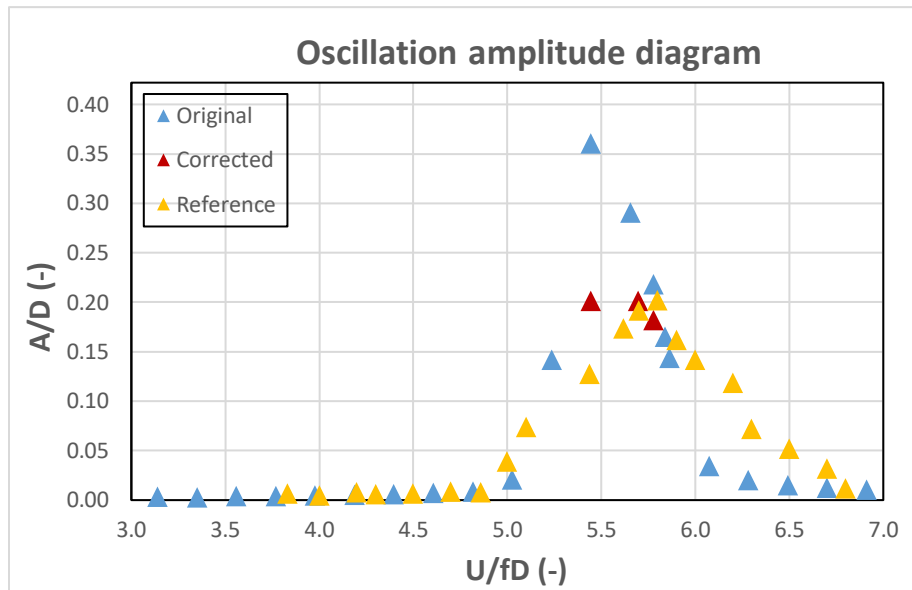
Figure 11: 2ⁿᵈ case scenario oscillation amplitude diagram

It is observed that the maximum A/D is 0.2 for $U/fD = 5.8$ with the corrected values, aligning with the anticipated result. Consequently, the prediction is now accurate. Additionally, the frequency ratio values are also shifted to the right, aligning with their expected positions.
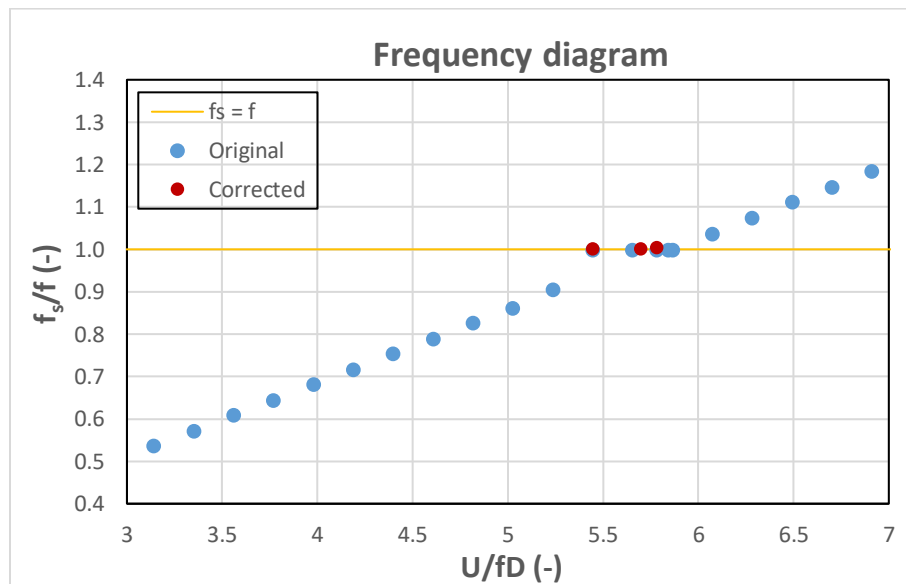
Figure 12: 2ⁿᵈ case scenario frequency ratio diagram

4.3.3 Concluding frequency ratio analysis: Case f$_s$/f = 1.24

In this case, the anticipated maximum amplitude value of the oscillation was determined to be different than the actual value indicated in Image 14. Additionally, this maximum value was set to be anticipated at a higher value of U/fD than the actual U/fD value indicated in the image. This information is represented in Table 19, with the highlighted values indicating those specifically referenced.

Table 19: Selected values for the 3rd case scenario

Variable	Value
$\omega_n \ (rad/sec)$	20.0
$f \ (Hz)$	3.18
$\omega_s \ (rad/sec)$	24.8
$f_s \ (Hz)$	3.95
f_s/f	1.24
U/fD	6.2
$U \ (m/s)$	2.96
A_y/D	0.16
$A_{target} \ (m)$	0.024

Following the application of the COBYLA optimization method, the dimensionless parameter values are as follows:

Table 20: Dimensionless parameters values (3rd case scenario)

G	G'	H	F
172.792271	6.967430282	81.125075	0.490675857

As the slight shift in the maximum amplitude values is observed again, the same correction procedure as in the previous case was applied. The parameters that occurred with COBYLA optimization method for three separate points in the lock-in region are as follows:

Table 21: Dimensionless parameters values (3rd case scenario)

U/fD	G	G'	H	F
5.7	116.843755	5.124726096	81.001297	0.53290327
5.9	140.080771	5.93562589	89.992397	0.571985574
6.1	161.199216	6.606525246	99.998881	0.614747219

The corrected values of G' and F are presented in Figure 13.
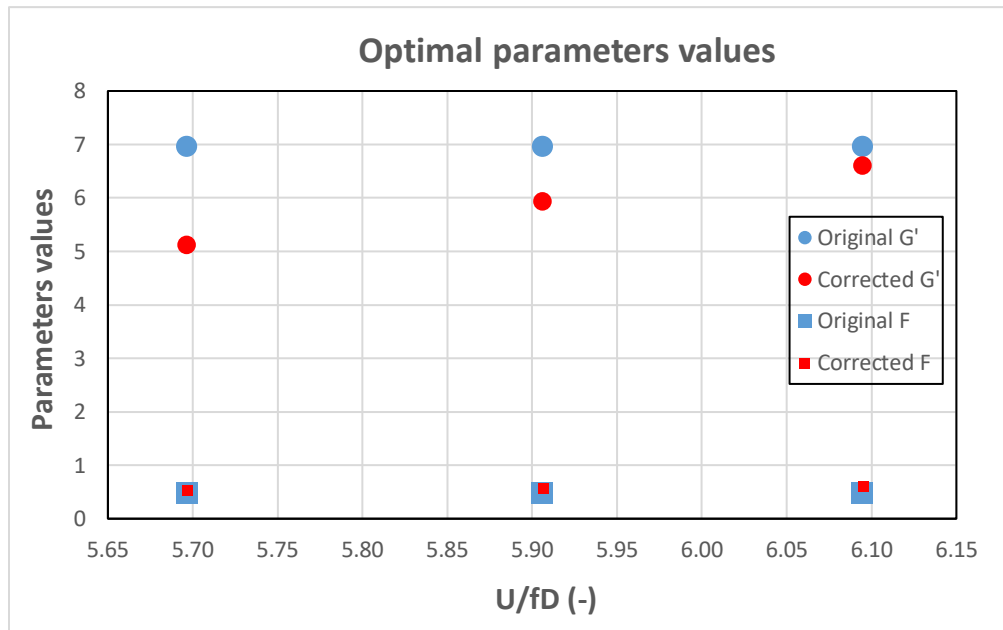
Figure 13: Corrected parameters values (3rd case)

The resultant plots are depicted below in Figures 14 and 15.
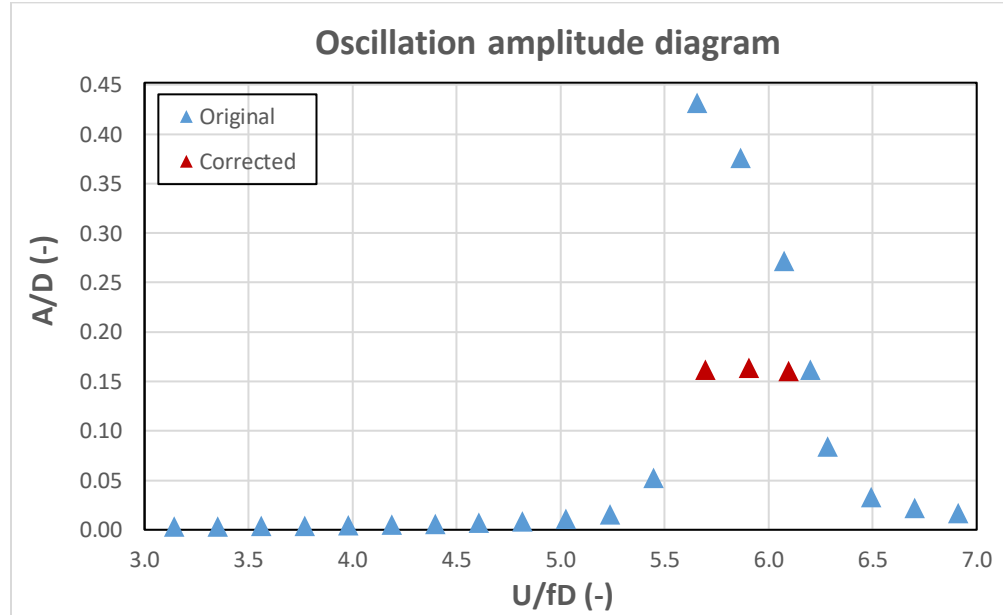
Figure 14: 3rd case scenario oscillation amplitude diagram

With the corrected version, it is now evident that the maximum A/D is 0.16 for $U/fD = 6.2$ as was anticipated. Consequently, the prediction is accurate.
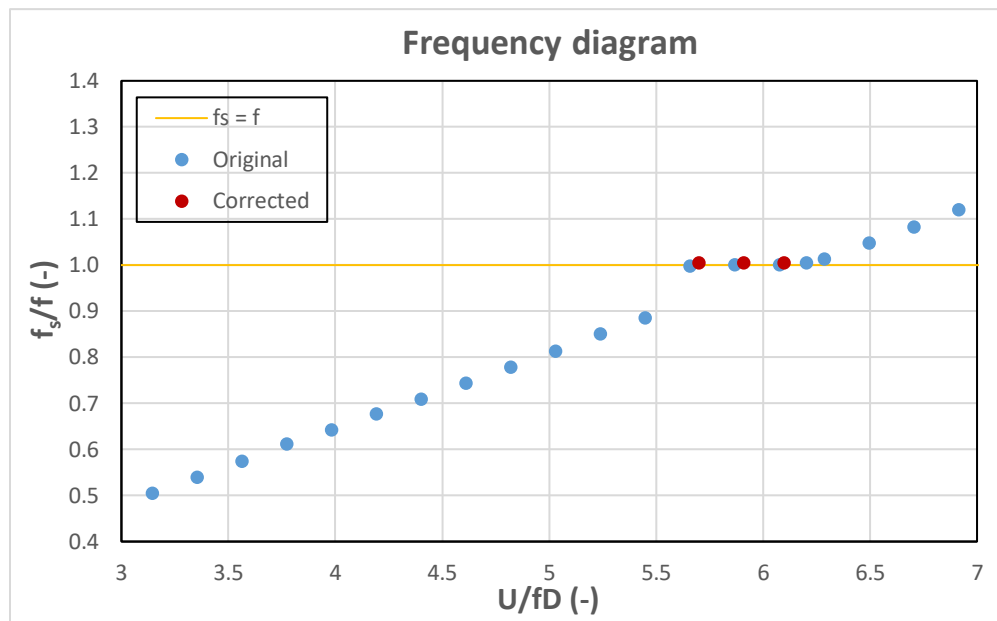
Figure 15: 3rd case scenario frequency ratio diagram

4.3.4 Comparison of the Cases

When comparing the three cases, it becomes evident that specific maximum values are targeted in each case scenario. These values are expected to be achieved at certain U/fD ratios. However, upon examination, it is apparent that while the targeted values are approximately attained in the results, they do not represent the maximum values of A/D. Instead, another maximum value (actual maximum value) is observed at a different U/fD. This actual value is notably higher than the targeted one and is shifted to the left as the U/fD value decreases. This information is depicted in Table 22.

The difference between the obtained value and the actual maximum value for every case shows a significant increase at the value of A/D and a decrease at the value of U/fD. Specifically, as the frequency ratio increases, the A/D values are getting higher, corresponding to U/fD values that are lower than the ones at which the targeted maximum A/D occurs. The deviation of increase for the A/D and the deviation of decrease for the U/fD are shown in Table 23.

Table 22: Actual values for every case

Case		$\frac{A}{D}$	$\frac{U}{fD}$	A_{target} (m)
A ($f_s/f = 1.0$)	Target max. value:	0.2	5.0	0.03
	Obtained value:	0.191	5.0	0.029
	Actual max. value:	0.285	4.6	0.043
B ($f_s/f = 1.16$)	Target max. value:	0.2	5.8	0.03
	Obtained value:	0.216	5.8	0.032
	Actual max. value:	0.359	5.4	0.054
C ($f_s/f = 1.24$)	Target max. value:	0.16	6.2	0.024
	Obtained value:	0.160	6.2	0.024
	Actual max. value:	0.430	5.7	0.064

Table 23: Deviation of obtained values from actual maximum values

Case	A/D		U/fD	
	Absolute deviation	Relative deviation	Absolute deviation	Relative deviation
A	0.093	48.7%	0.419	8.3%
B	0.142	65.7%	0.335	5.8%
C	0.270	168.9%	0.545	8.8%

The resultant plots for every case are depicted in the same diagram, in Figures 16 and 17.
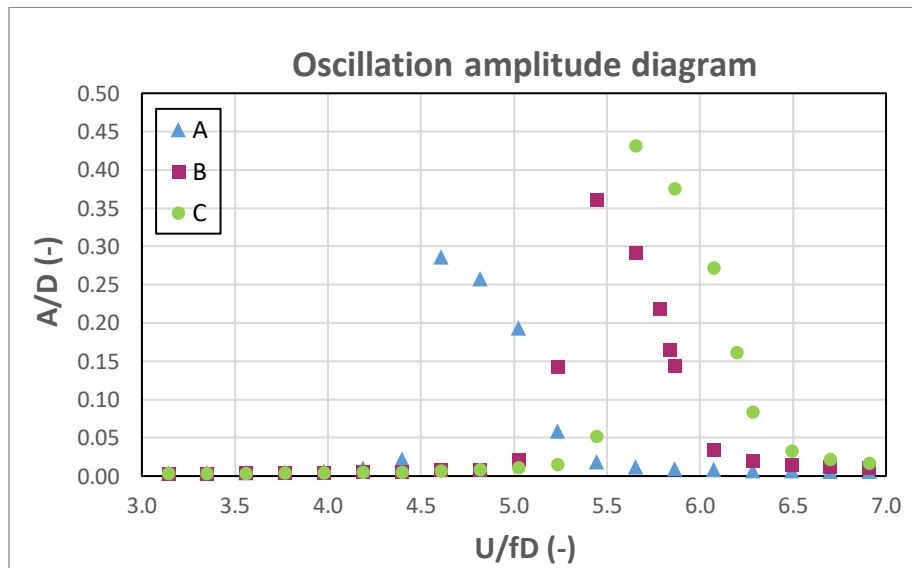
Figure 16: Oscillation amplitude diagram for all cases plotted together
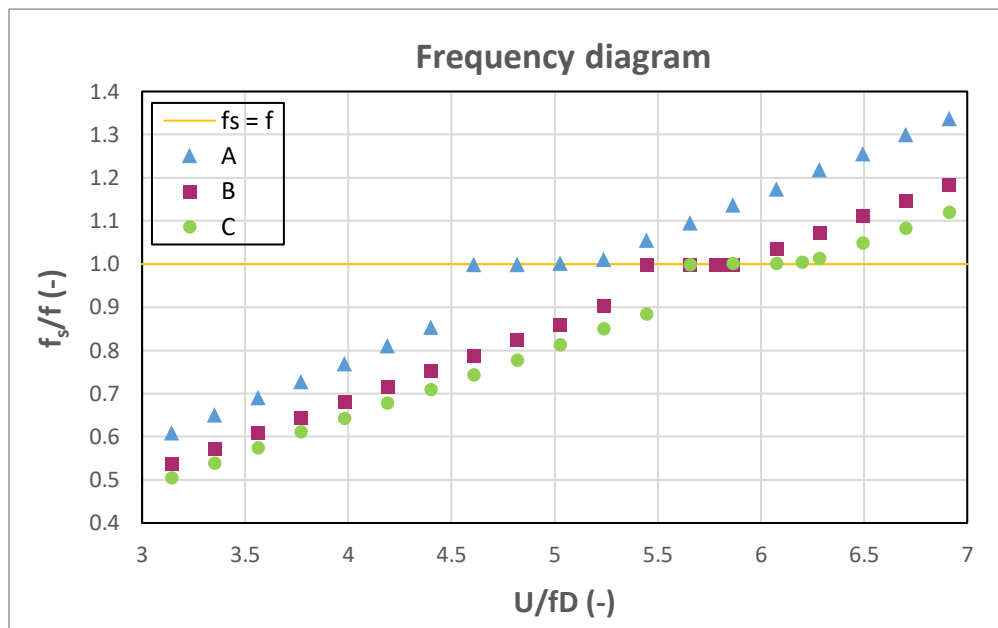
Figure 17: Frequency diagram for all cases plotted together

4.4 Automated Prediction using Linear Interpolation

In the subsequent procedure, a more automated approach was explored to predict the model's results and the behavior of each system. One straightforward method considered was to employ linear interpolation between certain optimal values of the parameters G and H. Subsequently, the model would be applied across a range of flow velocities, with the corresponding optimal values of G and H determined based on the desired velocity. To initiate this investigation, a flow velocity of $U = 2.6\,m/s$ was selected, and several cases with different natural frequencies were examined. For each natural frequency, a specific U/fD ratio was determined, and based on Image 14, the corresponding A/D value was derived. Using the COBYLA optimization method, a set of optimal values for the parameters G and H was obtained from this data.

Interestingly, it was observed that employing the model in a form utilizing the parameters G' and F, rather than G and H, leads to more accurate results. Therefore, after determining the optimal values of G and H, they were transformed into G' and F according to Equations (4.6) and (4.7) to facilitate linear interpolation. The resulting diagram depicting the G' and F parameters versus the U/fD values is presented in Figure 18.
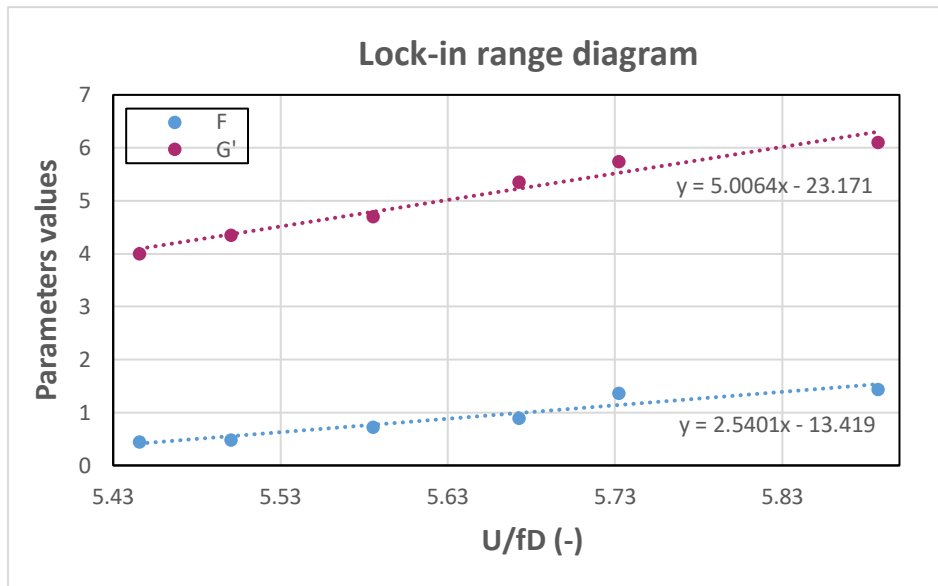
Figure 18: G' and F parameters versus U/fD values for the lock-in region

The model produced the blue spots depicted in Figure 19 by applying the linear interpolation procedure for the lock-in region. For the range of flow velocities before entering the lock-in region, the spots were determined by keeping the first values of the G' and F parameters constant, which were calculated from the linear interpolation. Consequently, the spots before this region were determined and colored dark pink in the same figure. Similarly, after the lock-in region, the last calculated values for the sets of parameters were kept constant, and then the region after the lock-in was calculated and colored green.
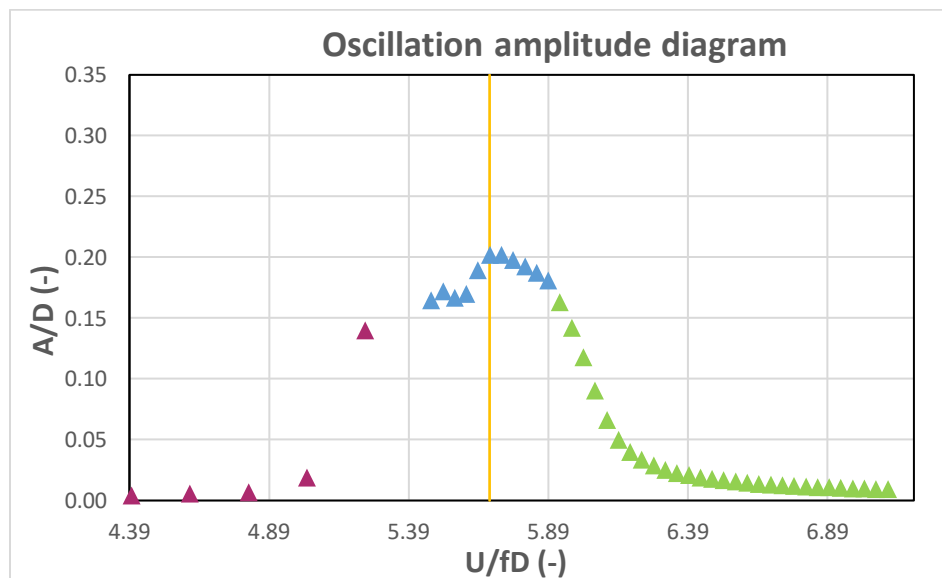
Figure 19: Displacement Prediction Using linear interpolation for the lock-in region

A yellow vertical line marks the actual maximum predicted value, which is accurately predicted by the model.

5. Conclusions

The thesis delved into understanding, analyzing, and predicting the Vortex-Induced Vibration (VIV) phenomenon in circular cross-section structures using both single-degree-of-freedom (1DOF) and two-degree-of-freedom (2DOF) engineering models. These models aimed to provide accurate predictions of VIV behavior across various velocity ranges.

Through rigorous examination, the 1DOF models were evaluated against the theoretical predictions of the Iwan Blevins model. While all 1DOF models demonstrated promising accuracy, a newly proposed model from the literature exhibited the closest alignment with theoretical predictions, showcasing its efficacy in capturing VIV behavior.

To fine-tune the 2DOF model, a meticulous optimization procedure was essential. Two optimization methods, Newton and COBYLA, were examined. Despite being slightly slower, the COBYLA method outperformed Newton's method in accuracy, establishing it as the preferred optimization technique for parameter refinement.

Exploring alternative prediction methodologies, two distinct approaches were pursued. Initially, the model's results were obtained by testing the optimal parameters produced by COBYLA in different frequency ratio case scenarios, revealing a phenomenon where the maximum amplitude value shifted slightly to the left.

Subsequently, an automated method was explored to predict the phenomenon more rapidly. This involved defining the values of dimensionless parameters for varying natural frequencies via individual COBYLA optimization runs. Then, linear interpolation was employed between the obtained parameter values for a range of velocities in the lock-in region. This method demonstrated sufficient accuracy.

In conclusion, the thesis emphasizes the importance of accurate prediction methodologies for VIV phenomena. Future research may focus on exploring other optimization methods and alternative engineering models and addressing discrepancies to improve predictive capabilities.

Furthermore, beyond future research directions, a more immediate and practical application lies in integrating the thesis findings into computational tools, such as the hGAST (Hydro-Servo-Aero-Elastic Simulation Tool), developed for comprehensive offshore wind turbine analysis. By incorporating optimization and linear interpolation techniques, the data obtained from predicting VIV phenomena can be integrated into the hGAST framework. Ultimately, this integration offers a more holistic understanding and prediction of the VIV phenomenon, applicable to large-scale engineering structures with complex dynamics.

6. List of Tables

7. List of Figures

8. List of Images

9. Bibliography

[1] G. Parkinson, "Phenomena and modelling of flow-induced vibrations of bluff bodies," in *Progress in Aerospace Sciences*, 1989, pp. 169-224.

[2] T. Sarpkaya, "A critical review of the intrinsic nature of vortex-induced," *JOURNAL OF FLUIDS AND STRUCTURES,* pp. 389-447, 26 January 2004.

[3] J. Parracho, "A Semi-Empirical Model for Vortex-Induced Vibrations of Tall Circular Towers," Lisbon, Portugal , 2012.

[4] A. D. M. F. K. S. Axelle Viré, "Two-dimensional numerical simulations of vortex-induced vibrations for a cylinder in conditions representative of wind turbine towers," *Wind Energy Science,* 23 June 2020.

[5] S. S. A. MeghanadhanC, "An Experimental Study of Vortex Shedding Behind a Bluff Body in a Water Channel," *International journal of engineering research and technology,* 2016.

[6] R. G. C.H.K. Williamson, " A brief review of recent results in vortex-induced vibrations," *Journal of Wind Engineering,* pp. 713-735, 2007.

[7] A. R. C.H.K. Williamson, "Vortex formation in the wake of an oscillating cylinder," *Journal of Fluids and Structures,* pp. 355-381, 1988.

[8] F. D. S. G. Z. A. Angrilli, " Hydroelasticity study of a circular cylinder in a water stream," 1972.

[9] O. R. Griffin, " The vortex-street wakes of vibrating cylinders," *Journal of Fluid Mechanics,* p. 553–576, 1974.

[10] E. Buffoni, "Vortex shedding in subcritical conditions," Physics of Fluids, 2003.

[11] S. S. S. Mittal, "Vortex-induced vibrations at subcritical Re," *Journal of Fluid Mechanics,* 2005.

[12] M. S. Pantazopoulos, "Vortex-Induced Vibration Parameters: Critical Review of the 13th International Conference on Offshore Mechanics and Arctic Engineering," USA, 1994.

[13] "TGDAMPERS.DK," [Online]. Available: https://tgdampers.dk/.

[14] M. P. S. K. Thomas Glen Ivanco, "Development and Validation of an Aeroelastic Ground Wind Loads Analysis Tool for Launch Vehicles," 2015.

[15] F. Rigo, "Generalized model for interacting cylinders in Vortex Induced Vibration," 2022.

[16] H.-J. N. R. H. o. Francesca Lupi, "Aerodynamic damping model in vortex-induced vibrations for wind," *Journal of Wind Engineering & Industrial Aerodynamics,* 2018.

[17] Y. Tamura, "Mathematical models for understanding Vortex-Induced Vibrations," 2020.

[18] R. B. W.D. Iwan, "A model for Vortex Induced Oscillation of Structures," *Journal of Applied Mechanics,* 1974.

[19] R. Blevins, Flow-induced vibration, New York: Van Nostrand Reinhold Company, 1977.

[20] C. M. R. J. M. Michel Hardika, "An improved van der Pol wake oscillator model for a 1DOF circular cylinder undergoing vortex induced vibrations," *European Journal of Mechanics / B Fluids,* 2024.

[21] Y. S. Y. L. M. L. M. L. H. L. Tianyi Zhang, "Vortex-induced vibration of a flexible rectangular cylinder: Experimental investigation and comparative study of theoretical models," *Journal of Wind Engineering & Industrial Aerodynamics ,* 2022.

[22] P. B. C. K. Vikas Khare, Tidal Energy Systems - Design, Optimization and Control, 2019.

[23] J. P. George Lindfield, Numerical Methods (Fourth edition), 2019.

[24] B. K. J., Finite element procedures, Prentice-Hall, Inc., 1996.

[25] C. Feng, "The measurement of vortex-induced effects in flow past stationary and oscillating circular and D-section cylinders," 1968.

[26] H. B. R.D. Gabbai, "An overview of modeling and experiments of vortex-induced vibration of circular cylinders," *Journal of Sound and Vibration,* 2005.

[27] G. Schewe, "On the force fluctuations acting on a circular cylinder in crossflow from subcritical up to transcritical Reynolds numbers," *Journal of Fluid Mechanics,* pp. 265-285, 1983.

[28] P. W. J. J. R. R. A. M. Ruben E. Perez, "pyOpt: a Python-based object-oriented framework for nonlinear," 2011.

[29] S. Community, "SciPy v1.12.0 Manual," [Online]. Available: https://docs.scipy.org/doc/scipy/reference/optimize.minimize-cobyla.html.

[30] J. J. M. a. D. C. Sorensen, Newton's Method, ILLINOIS.

[31] K. X. Γιαννάκογλου, Μέθοδοι Βελτιστοποίησης στην Αεροδυναμική, 2006.